Influences of Indian and Pacific Ocean Coupling on the Propagation of Tropical Intraseasonal Oscillation

Shu-Ping Weng*[1] and Jin-Yi Yu[2]

[1]Department of Geography, National Taiwan Normal University, Taipei, Taiwan
[2]Department of Earth System Science, University of California, Irvine, USA

A manuscript submitted to the journal of

Climate Dynamics

(Submitted: 21 December, 2006; Revised: 3 August, 26 September, 2007)

[1] *Corresponding Author address: Dr. Shu-Ping Weng, Department of Geography, National Taiwan Normal University, Taipei, Taiwan. Tel: 886-2-23637874-133, Fax: 886-2-23691770, Email: znspw302@ntnu.edu.tw.

ABSTRACT

This study examines the influences of Pacific and Indian Ocean coupling on the propagations of tropical intraseasonal oscillation (ISO) in boreal winter (November-April) and summer (May-October). A series of three basin-coupling experiments are performed with the UCLA CGCM, in which the air-sea coupling is limited to the Indian Ocean, the Pacific Ocean, or both the Indian and Pacific oceans. Using extended EOF and composite analyses, the leading ISO modes are identified and compared between the observations and the model experiments. Results show that the Indian Ocean coupling is an important part of ISO generation mechanism in both the winter and summer seasons. Without the coupling, the intensity of simulated ISO is considerably reduced. As for the propagation characteristics, this study finds the Pacific Ocean coupling important to the zonal propagation of wintertime ISO and the Indian Ocean coupling crucial to the meridional propagation of summertime ISO. Without the Pacific Ocean coupling, the eastward propagation of the wintertime ISO is mostly restricted within the Indian Ocean sector. Lacking of the Indian Ocean coupling, the simulated ISO in boreal summer cannot propagate northward into the Asian-Pacific monsoon regions.

To further identify the role of the ocean coupling, a series of AGCM experiments are performed with their SSTs prescribed from the climatology produced in the basin-coupling experiments. It is found that the ocean couplings promote the ISO propagation by configuring a proper phase relationship between its surface fluxes, winds, convection, and the underlying SST fluctuations. In this particular CGCM, the couplings affect ISO convections mainly through the wind-evaporation feedback rather than the cloud-radiation feedback, while in observations both processes are equally important.

(*Keywords*: Intraseasonal oscillation, Atmosphere-ocean coupling, MJO, Indo-Pacific climate variability, Basin-coupling experiments)

1. Introduction

Since the pioneering work of Madden and Julian (1971, 1972), tropical intraseasonal oscillation (ISO) has been increasingly recognized as a phenomenon important to both climate and weather. This phenomenon is characterized by large-scale convection and circulation anomalies, propagating primarily eastward along the equator and with broad timescales of 20-90 days. Observational studies have revealed that large fluctuations occur in sea surface temperature (SST) associated with the passage of ISO in the Indo-Pacific warm pool (e.g., Krishnamurti et al. 1988; Zhang 1996, 1997; Weller and Anderson 1996; Lau and Sui 1997; Hendon and Glick 1997; Woolnough et al. 2000, and others). In the recent Bay of Bengal Monsoon Experiment (BOBMEX; Bhat et al. 2001) and Joint Air-Sea Monsoon Interactive Experiment (JASMINE; Webster et al. 2002) field experiments, SST anomalies (SSTA) induced by the summertime ISO were found to be as large as 2°C in individual cases. The coherent fluctuations between ISO and SST have prompted the notion that the atmosphere-ocean coupling is an essential element of the tropical ISO dynamics (see Wang 2005 for a comprehensive review of the ISO dynamics).

The propagation characteristics of ISO in the Indo-Pacific sector were noticed to change in accord with the seasonal variation of SST distribution. Figure 1 shows the Indo-Pacific SST climatology (1981-2001) in boreal winter (November-April; NDJFMA) and summer (May-October; MJJASO) calculated from NOAA Optimum Interpolation SST (OISST_v2; Reynolds et al. 2002). In winter (Figure 1a), the SST distribution is more or less symmetric to the equator, with warm

SSTs (>27°C) concentrated along the equator and extending from the eastern Indian Ocean to east of the dateline. Observations showed that, in this season, the ISO propagation is predominantly eastward. After being initiated in the western Indian Ocean, the ISO passes through the Maritime Continent, redevelops over the western Pacific warm pool, and often intersects the South Pacific convergent zone (SPCZ) where the warm SSTs reside (Wang and Rui 1990; Jones et al. 2004). In boreal summer (Figure 1b), the Indo-Pacific warm SSTs shift more northward and become asymmetric to the equator. The warm waters cover the entire Northern Indian Ocean and reach 20°N in the western Pacific region. The eastward extension of the warm water retreats to the dateline. In this season the eastward ISO propagation weakens substantially as it approaches the Maritime Continent (e.g., Kemball-Cook and Wang 2001). A northward (or northwestward) propagation branch of the ISO becomes prominent in the Asian-Pacific monsoon regions (Yasunari 1980, 1981; Krishnamurti and Subrahmanyam 1982; Lau and Chan 1986; Wang and Rui 1990; Hsu and Weng 2001; Hsu et al. 2004).

Coupled atmosphere-ocean models of various complexities had been used to study the importance of the ocean coupling to ISO. The results have not been conclusive and appear model dependent. However, many studies found that the coupling enables the employed models to produce more realistic ISO simulations, indicating the importance of the coupling to the ISO. Wang and Xie (1998) coupled a simple atmospheric model to a mixed-layer ocean and showed that intraseasonal SST variations can affect surface pressure and thus enhance or reduce ISO convective activity. They argued that the coupling could destabilize the atmosphere for the growth of ISO. The coupling also slows down the propagation speed of the simulated

ISO and allows their simple coupled model to produce more realistic ISO simulations. Waliser et al. (1999) coupled a slab ocean model to the GLA general and also found the ocean coupling improves the ISO simulations. Watterson (2002) used the CSIRO Mark2 Coupled atmosphere-ocean GCM (CGCM) to examine the sensitivity of ISO to model ocean configurations. His results showed that the coupling increases the amplitude and propagating speed of the model ISO. With a fully coupled HadCM3 CGCM, Inness and Slingo (2003) showed that many observed ISO features can be captured in the coupled simulation but not in the uncoupled AGCM simulation prescribed with observed SSTs. Fu and Wang (2004) further demonstrated the importance of SST feedback to ISO evolutions. They coupled the ECHAM4 AGCM to an intermediate ocean model and showed that this hybrid-coupled model can produce realistic propagating ISO. But when they forced the same AGCM with the simulated SST produced from the coupled run, the model produces erroneous standing oscillation. Zhang et al. (2006) performed several pairs of CGCM and AGCM experiments to show that the ocean coupling generally strengthens the simulated propagating ISO signal. Recently, Watterson and Syktus (2007) found the responsiveness of model mixed layer in the Pacific warm pool crucial for providing a sufficient SST response to help the ISO propagate through the Maritime Continent into the western Pacific.

One important issue not addressed in these coupled modeling studies is the individual roles of the Pacific and Indian ocean coupling to the ISO. These two oceans have different mean surface temperature distributions and opposite mean surface wind directions associated with the Pacific and Indian cells of the Walker circulation. The couplings over these two oceans might affect the ISO differently. In particular, the boreal winter ISO propagates across both the Indian and Pacific oceans, while the summer ISO propagates northward mostly inside the Indian Ocean sector. Would it be possible that the Pacific coupling more important to the wintertime ISO propagation and the Indian Ocean coupling more important to the summertime ISO propagation? To answer these questions, this study contrasts the ISO simulations produced from a series of three basin-coupling CGCM experiments in which the atmosphere-ocean coupling is limited, respectively, to the tropical Pacific Ocean, tropical Indian Ocean, and both the tropical Pacific and Indian oceans. In addition to the atmosphere-ocean coupling, the basic state biases in coupled models also affect their ISO simulation (Inness and Slingo 2003; Zhang et al. 2006; Watterson and Syktus 2007). When the observed SSTs are prescribed, the model's basic state biases are usually smaller. Therefore, our basin-coupling methodology helps to reduce the model biases in one ocean basin while the importance of the coupling in the other ocean basin is examined. To further separate the effects of atmosphere-ocean coupling and basic state bias on ISO simulations in the CGCM experiments, we also performed a series of AGCM experiments in which the SSTs are prescribed with the monthly climatologies produced by the basin-coupling CGCM experiments.

This paper is organized as follows. The basin-coupling methodology and the CGCM used in this study are described in Section 2. The simulated ISO during the boreal winter and summer seasons are contrasted with the observations in Sections 3 and 4, respectively. Results of the forced AGCM runs are contrasted with their coupled counterparts in Section 5. Section 6 summarizes the major findings of this study.

2. Model and basin-coupling experiments

The CGCM (detailed in Yu and Mechoso 2001) used in this study consists of the UCLA AGCM (Mechoso et al. 2000) and GFDL Modular Ocean Model (MOM; Bryan 1969; Cox 1984). The AGCM has a global coverage with a horizontal resolution of 4° in latitude and 5° in longitude and 15 levels in the vertical with the top at 1-mb. The OGCM has a longitudinal resolution of 1° and a latitudinal resolution varying gradually from 1/3° between 10°S and 10°N to about 3° at both 30°S and 50°N. It has 27 layers in the vertical with 10-m resolution in the upper 100 –meters. The AGCM and OGCM are coupled daily without flux correction. Three basin-coupling experiments are performed: the Pacific Ocean (PO) Run, the Indian Ocean (IO) Run, and the Indo-Pacific (IP) Run. In the PO Run, CGCM includes only the tropical Pacific Ocean (30°S-50°N, 130°E-70°W) in its ocean model domain. The IO Run includes only the tropical Indian Ocean (30°S-50°N, 30°-130°E) whereas the IP Run includes both the tropical Indian and Pacific oceans (30°S-50°N, 30°E-70°W) in the ocean model domain. Outside the ocean model domains, climatological monthly SSTs are prescribed. Inside the ocean model domains, SSTs polarward of 20°S and 30°N are relaxed toward their climatological values. The IP, PO, and IO Runs were integrated for about 60 years. Only the last 30 years of the integrations is analyzed in this study. The observed ISO properties in circulation and convection fields are derived respectively from the daily-mean European Re-Analysis product (ERA-40; Uppala et al. 2005) and the pentad-mean CPC merged analysis of precipitation (CMAP; Xie and Arkin 1997) in their overlapped period of 1979-2001.

We compare in Figure 1 the observed OISST_v2 (Figs. 1a and 1b) climatology and the simulated SSTs from the IP Run (Figs. 1c and 1d). The general patterns of the observed Indo-Pacific SST distribution are reasonably captured in the simulation. The simulated warm pool covers both the western Pacific Ocean and the eastern Indian Ocean. A cold tongue is produced in the eastern equatorial Pacific with its strength stronger in MJJASO than in NDJFMA. The northward extension of the warm SSTs in the Indian Ocean during the boreal summer is realistically simulated. Similar northward extension is also produced in the western North Pacific, even though it does not extend as far north as in the observation. Although the gross features are quite realistic, this model tends to produce SSTs that are too cold in the Indian Ocean and too warm in most areas of the tropical Pacific Ocean. Other model deficiencies include a warm bias in the eastern Pacific north of the equator, a too zonal and too eastward extension of the southern branch of western Pacific warm pool, and a cold bias around the Maritime Continent. The two warm biases are associated with the so-called double ITCZ problem that many contemporary CGCMs face (Mechoso et al. 1995). The cold bias around the Maritime Continent is particularly serious in NDJFMA (Fig. 1c). The observed zonal elongation of the Indo-Pacific warm pool is interrupted in this area. The IO and PO Runs produce SST climatologies (not shown) similar to those of the IP Run, except that the IO Run has a larger cold bias in the Indian Ocean and the PO Run has a larger warm bias in the Pacific Ocean as compared to the IP Run.

To extract ISO signals, we adopt the procedure used by Rui and Wang (1990). The mean annual cycle is first removed from daily data to produce daily anomalies. A 3-month running mean anomaly, which estimates the subannual-to-interannual variation, is then removed from the daily anomaly before computing the 5-day mean pentad anomaly. This band-pass filtering procedure retains intraseasonal variations with timescales ranging from 10 days to 3 months. The CMAP precipitation dataset is also processed in a similar way but taking its pentad-resolution into account. Figure 2 compares the variance of the coupled model simulated (colored solid lines) and observed (black solid lines) filtered anomalies in 850-mb zonal wind (U'_{850}) averaged between 10°S and 10°N in both NDJFMA and MJJASO. In the observations, the winter variance concentrates in the region from the central Indian Ocean to the west of dateline. The variability decreases rapidly toward the eastern Pacific. The maximum variance appears in the western Pacific warm pool. In summer, the observed variance spreads over a wider longitudinal range, with large variance extending into the eastern tropical Pacific and the variance maximum shifting westward into the Indian Ocean. Although the model variances are too small, all three model experiments produce variance distribution and its seasonality similar to the observed. Among the experiments, the IO Run produces larger intraseasonal variance than the other two runs in both seasons. In particular, only the IO Run captures the double peaks of the summer variance observed in the eastern Indian Ocean and western Pacific Ocean.

3. Boreal winter ISO propagation

To identify the dominant ISO mode and its propagation characteristics, an Extended Empirical Orthogonal Function Analysis (EEOFA; Weare and Nasstrom 1982) is applied to filtered easterly vertical shear (EVS) anomalies in the tropical eastern hemisphere (20°S-20°N, 30°E-180°E) where the intraseasonal variance is concentrated. A 5-pentad lead-lagged window is used in the EEOFA. Here the EVS is defined as the difference between the anomalous zonal winds at 200-mb and at 850-mb (U'_{200}-U'_{850}). This quantity gives a good measurement of the strength of the gravest baroclinic mode associated with the large-scale deep convections (Wang and Fan 1999). We find applying the EEOFA to the EVS anomalies particularly effective in isolating the ISO from the model experiments where the intraseasonal variability is weak. Choice of this quantity is also in accord with the recent suggestion of Wheeler and Hendon (2004) that ISO is best identified when an EOF analysis is applied to the combined U'_{200}, U'_{850}, and the outgoing longwave radiation anomalies together.

In NDJFMA, the percentage of the 10-to-90days EVS variance explained by the first (second) EEOF mode is 14.0% (13.6%), 12.3% (11.8%), 9.5% (8.8%), and 16.0% (15.3%) for the ERA-40, IP, PO, and IO Runs, respectively. Since the lagged covariance matrix is constructed, the propagating patterns are identified as pairs of degenerate eigenvectors that are approximately in quadrature. For the sake of discussion, only the half cycle of the first EEOF mode from the observed EVS evolution is shown in the left panels of Figure 3. A convergent (divergent) zone in the 850-mb level is denoted at the zero contour line of EVS with positive (negative) anomalies to its right and negative (positive) anomalies to its left. The figure shows that the leading winter ISO mode is characterized by an eastward propagating wavenumber 1 structure with an innegligible wavenumber 2-to-3 component embedded. The evolutions of ISO in other field are then averaged from the 40 most extreme (with 20 positive and 20 negative) ISO events. These events are selected based on the principal component of the first EEOF mode. Recent studies showed that the canonical ISO activity could be modified over the course of Asian-Australian summer monsoon seasons in response to the seasonal migration of the warmest SSTs (e.g. Kemball-Cook and Wang 2001; Watterson and Syktus 2007). Behaviors of ISO can be different between the onset month and the final month. But this is not a concern to our composite, because most of the extreme events we composite are found to occur in the mid-season periods of December-March (80%-90%) and June-September (88%-93%).

Figure 4 shows the Hovmöller diagrams of the composite ISO life cycle in 200-mb velocity potential anomalies (χ'_{200}) along the equator (10°S-10°N). The observed χ'_{200} (Figure 4a) is characterized by an eastward-propagating wavenumber 1 pattern that circumnavigates the globe in about 50 days. In all the three model runs, the simulated ISOs have smaller amplitudes than observed (note the different contour intervals used in Figures 4a and 4b-d). Nevertheless, the IP Run (Figure 4b) reproduces well the observed eastward propagation of ISO. The IO Run (Figure 4d) produces strong ISO activities in the Indian Ocean with an obvious eastward propagation, although the propagation speed is slower than the observation. However, the ISO propagation is limited in the Indian Ocean. It is noticed that the ISO amplitude diminishes dramatically near 130°E, which is the eastern boundary of the active Indian Ocean in the IO Run. Without the Indian Ocean coupling, the PO Run (Figure 4c) still shows an indication of eastward ISO propagation in the Indian Ocean. But the simulated ISO amplitude is very weak in this sector. The simulated ISO is enhanced significantly in the western Pacific Ocean and propagates eastward continuously. The modeling results indicate that the generation of wintertime ISO over the Indian Ocean sector depends on the local atmosphere-ocean coupling. The results also suggest that the Pacific Ocean coupling is crucial to sustain the eastward propagation of the wintertime ISO. Without this coupling, the strong ISO produced by the IO Run in the Indian Ocean sector cannot propagate into the Pacific Ocean sector. Only when the couplings coexist in both the Pacific and Indian oceans can the IP Run reproduce an ISO mode that has equivalent peak intensity between the Indian Ocean and western Pacific and a more realistic eastward propagation.

Embedded in the eastward ISO propagation that simulated by the IP Run are two standing oscillations that do not exist in the observations. One of them is located at 60°E and the other at 180°E. These oscillations appear as local enhancements of ISO amplitudes. The standing oscillation at 60°E gets stronger in the IO Run but weaker in the PO Run, whereas the standing oscillation at 180°E is the largest in the PO Run but is absent from the IO Run. These results suggest that these unrealistic standing oscillations are likely related to model deficiencies caused by the coupling in the central Indian and Pacific oceans. We notice from Figure 5 that the CGCM runs produce significant biases in the low-level (850-mb) winds over these two regions. In this figure, tropical westerlies are highlighted as red vectors. Figure 5a shows that westerlies prevail between the central Indian Ocean and the western Pacific warm pool in the observations. The IP Run (Figure 5b) produces prevailing westerlies in the regions similar to those observed. However, it is noticed that the intensity of model westerlies reduces significantly when they approach Sumatra. The westerlies also extend too far eastward and are too strong in the central Pacific. These biases result in unrealistic low-level convergence in the regions close to where the standing ISO oscillations of χ'_{200} are produced. The westerly bias in the Indian Ocean is most serious in the IO Run (Figure 5d), in which the westerlies even reverse to easterlies in the eastern Indian Ocean. As mentioned, this run has the most serious standing oscillation at 60°E among the three runs. The PO Run (Figure 5c) does not have a serious wind bias problem in the Indian Ocean; neither did this run produce a large standing oscillation at 60°E. As for the wind bias of the central Pacific, it occurs in the PO run but is less obvious in the IO Run because the SSTs therein are prescribed from observations. This is consistent with the fact that the standing oscillation at 180°E exists in the PO Run but is absent from the IO Run. Figures 4 and 5 together suggest that the erroneous standing oscillations are caused by the model biases in the mean surface wind simulations. We can further link the wind biases to the SST biases discussed in Figure 1. The cold bias around the Maritime Continent can result in a local high-pressure anomaly from which low-level winds diverge westward and lead to the weakening of the westerlies in the central Indian Ocean. The too-eastward extension of the western Pacific warm pool, on the other hand, enhances and extends the westerlies into the central equatorial Pacific, where they encounter the Pacific easterlies and thereby result in an unrealistic convergence near the dateline.

We further compare in Figure 6 the observed and simulated ISO life cycles in rainfall and 850-mb wind anomalies. Only the first half of the life cycle is shown. The other half cycle is similar but with opposite signs. The color-shaded areas and black vectors denote respectively the rainfall and wind anomalies significant at 95% and 90% confidence levels. The observed rainfall anomalies (Figure 6a) show a four-stage development process: 1) initiation over equatorial Africa and/or western Indian Ocean (phase 1); 2) rapid intensification when passing through the Indian Ocean (phases 1-3); 3) mature evolution characterized by a weakening in the Maritime Continent and redevelopment over the western Pacific (phase 3-5); and 4) dissipation when approaching the dateline in moderate events or emanating from the equator toward North America and southeastern Pacific in strong events (phase 6).

Associated with the positive rainfall anomalies, the major features in the low-level wind field include: 1) a concentrated westerly anomaly and a pair of off-equator cyclonic circulations coupling with enhanced rainfall anomalies in between propagate eastward; 2) a convergent center that leads the maximum rainfall during the developing and mature phases; and 3) a maximum westerly anomaly that lags rainfall anomalies during the developing phase but almost overlaps during the mature phase and leads the rainfall anomaly in dissipation phase. These features have been reported by several observational studies (e.g., Rui and Wang 1990; Jones et al. 2004).

In the IP Run (Figure 6b), although the significant area in the tropical warm waters is much smaller than the observations, the model ISO life cycle captures many observed features well. Rainfall anomalies initiated in the equatorial Africa and propagating eastward from the Indian Ocean to the Maritime Continent are reproduced (phases 1-3). Meanwhile, the associated intensified equatorial westerly (easterly) anomalies also tend to lag the enhanced (suppressed) rainfall anomalies during this developing phase (Hendon and Salby 1994; Zhang et al. 2006). Moreover, the enhanced rainfall and the lagged westerly anomalies are capable of passing through the Maritime Continent from the south and then head toward the central Pacific (phases 4-6). The redevelopment of the ISO in the western Pacific warm pool (phase 3-4) and its later intersection with the SPCZ (phase 5-6) are also faithfully reproduced in the IP Run.

Dramatic changes occur in the PO Run (Figure 6c) when the Indian Ocean coupling is absent. Firstly, there is little evidence of eastward propagating rainfall anomalies followed by the wind anomalies in the equatorial Indian Ocean. Instead, rainfall anomalies are stalled over the western Indian Ocean. The somewhat retrograded westerly anomalies over the equatorial eastern Indian Ocean and Maritime Continent can be interpreted as parts of the upstream atmospheric change in the low-level branch of Walker cell in response to the intraseasonal SSTA forcing over the warm pool-SPCZ region. It thus suggests that the appearance of mean westerly winds (evident in the PO Run) is only a necessary condition for sustaining a realistic ISO event. Secondly, without the coupling in the Indian Ocean, the PO Run produces a weaker ISO over the western Pacific due to the lack of ISO propagating in from the Indian Ocean. Although having a slower pace and being more confined within the Indian Ocean, rainfall and low-level circulation anomalies in the IO Run (Figure 6d) resemble those in the IP Run until they are approaching Sumatra in phase 4. It is in this location that the basic-state westerly winds diminish and change into easterlies. This result supports the paradigm of Inness and Slingo (2003) that the dismissal of mean westerlies near the Maritime Continent in CGCM signifies the climatic barrier for ISO in its voyage towards the western Pacific.

Figure 7 shows the evolutions of the SSTA associated with the composite ISO lifecycle in the observations and the IP Run. The ISO-related SSTA in the PO and IO Runs are similar to those in the IP Run in the interactive ocean basins and are not shown. In observations, the SSTA show an eastward propagating pattern from the western Indian Ocean to the dateline. For the sake of comaprison, centers of the enhanced rainfall anomalies in Figure 6 are marked as open triangles in Figure 7. It is clear that the propagation of SSTA is in accord with the that of the ISO rainfall anomalies. The enhanced rainfall anomalies are preceeded by positive SSTA and followed by negative SSTA by 2-3 pentads (Waliser et al. 1999; Woolnough et al.

2000).These phase relationshsips suggest that the eastward propagation of the ISO convection could be helped by the destablization effect produced by the positive SSTA to its east (Wang and Xie 1998). At the same time, the enhanced ISO convection activity forces negative SSTA to its west. The observed SSTA diminish as they approach the dateline. Although still not comparable to observations, the IP Run reproduces a considerable 0.2℃-0.3℃ magnitude in the ISO-related SSTA (Figure 7b). In the Indian Ocean, there exist statistically significant SSTA propagating eastward along the equator. It is in the western Pacific warm pool and SPCZ regions that the model simulates a comparable magnitude of SSTA as observed. In these regions, southeastward migration of positive SSTA capable of crossing the dateline is particularly clear. This would facilitate the subsequent rainfall pattern to further propagate eastward as seen in Figure 6b. Although inconsistencies exist, simulated phase relationships between the SST and rainfall anomalies resemble the observations, suggesting that the gross features of observed ISO-SST interactions are captured by this CGCM.

We further analyze the surface heat fluxes asscoaited with the composite ISO to examine how the ISO-SST interactions are produced. Figure 8 shows the composite latent heat fluxes (LHF; shadings) and short wave radiation (SWR; contours) from observations and the IP run. The sign is positive downward. Consistent with previous studies (e.g., Woolnough et al. 2000), other heat flux terms are found less important to the SSTA (not shown). In the observation (Figure 8a), compabale maginitudes of LHF and SWR anomalies migrate eastward across the Maritime Continent and into the western Pacific. Centers of SWR anomalies almost coincide with those of rainfall anomalies with enhanced rainfall anomalies accompanied by reduced SWR anomalies and vice versa (Inness and Slingo 2003). As for the LHF anomalies, their phase relations with the rainfall anomalies change as the ISO propagates from the Indian Ocean to the western Pacific. When it is in the Indian Ocean (phases 1-3), the enhanced rainfall anomalies are associated with the negative LHF anomalies (i.e., increased evaporation) to the west and positive anomalies (i.e., reduced evaporation) to the east (Woolnough et al. 2000; Inness and Slingo 2003). This in-quaradture phase relation can be explained as a result of convection-wind-evaporation process. The moisture convergence induced by the convection produces westerlies to the west and easterlies to the east of the rainfall center (see the wind vectors shown in Figure 6). Superimposed on the mean surface westerlies in the Indian Ocean, these wind aomalies increase wind speed to the west but decrease it to the east. Evaporation is thus enhanced to the west but weakened to the east of the enhanced rainfall center. When the ISO propagates into the western Pacific where the mean surface winds become easterlies, the easterly anomalies to the east of the rainfall center lead to a stronger total wind speed and give rise to an enhanced evporation (i.e., negative LHF anomaloies). As a result, the area of negative LHF anomalies expands and becomes overlapped with the enhanced convections as well as the negative SWR anomalies. Centers of LHF and SWR anomalies become coincide with each other in phases 4-6. Therefore, anomalies in these two flux terms are in-quadrature in the Indian Ocean but roughly in-phase in the Pacific Ocean (Zhang and McPhaden 2000; Inness and Slingo 2003). The positive (negative) SSTA center shown in Figure 7 [marked as +(－) in Fig. 8] basically follows the center of the positive (negative) LHF anomalies in both the Indian and Pacific oceans. It is in the western Pacific Ocean that the SWR anomalies become important to prolong the duration of SSTA, consistent with the results of some other CGCMs (e.g., Cubucku and Krishnamurti 2002). As the ISO propagates into the SPCZ and encounters the semi-perminant cloudiness, the SSTA (and thus ISO convections) disappear in response to the decaying SWR anomalies. In the IP Run, the SWR anomalies are much smaller and less organized as compared to the LHF anomalies. The simulated ISO-related SSTA appear to be mainly driven by LHF anomalies. Similar SST-LHF relationships are also found in the PO and IO Runs over their interactive ocean domains (not shown).

Results from Figures 7 and 8 suggest that the wind-evaporation-SST interaction is a major mechanism that allows ISO to perturb the Indo-Pacific SSTA which later help to promote the eastward propagation of the opposite phase of the ISO cycle. The SWR-SST interaction is another important mechansim to promote the ISO-SST interaction in the observations but is not captured by this CGCM.

4. Boreal summer ISO propagation

The evolution of summertime ISO is mainly described by the first two EEOF modes which together explain 21.1%, 16.6%, 14.9%, and 20.1% of the total variance of EVS anomalies for the ERA-40, IP, PO, and IO Runs, respectively. Compared to the percentages obtained in boreal winter (27.6%, 24.1%, 18.3%, 31.3%), the variances explained by the summertime ISO are lower in both the observations and the model runs. The right panels of Figure 3 show the observed EVS evolution in the half-cycle of the leading EEOF mode. Similar to its wintertime counterpart, a large-scale eastward propagation is found in boreal summer. Unlike its wintertime counterpart, a northward propagation branch is signified by a northwest-to-southeast tilting in the zero contour line of EVS anomaly.

Figure 9 shows the composite χ'_{200} (averaged between 14°N and 2°S). In observations (Figure 9a), three active centers with enhanced anomalous amplitude appear when the χ'_{200} pattern propagates eastward: the Arabian Sea-western coasts of Indian subcontinent (60°E-75°E), the Maritime Continent-western Pacific (120°E-150°E), and the eastern tropical Pacific-Central America (120°W-90°W). When approaching these regions, the ISO propagating speed also slows down. Although the third center appears to be minor, it stands out as a major center in the low-level circulation and convection fields. The center in the Indian Ocean is well captured in the IP Run (Figure 9b) and is best reproduced in the IO Run (Figure 9d), but is absent from the PO Run (Figure 9c). The IO Run reproduces the eastward propagation of this center most realistically, although there is a weak standing component embedded in its propagation. The Maritime Continent-western Pacific center is simulated by all three model runs. However, the PO Run has the strongest intensity and the IP Run captures the eastward propagation more realistically. The PO Run produces an erroneous standing oscillation component which overpowers the eastward-propagation component around the Maritime Continent-western Pacific center. All three runs produce a too strong standing component at the eastern tropical Pacific-Central American center.

Figure 10 shows the evolutions of the composite ISO life cycle in 850-mb wind and rainfall anomalies. The observed ISO (Figure 10a) shows distinct features from its wintertime counterpart. Rainfall anomalies that initiate near the coasts of equatorial East Africa in phase 2 propagate eastward along the equator before arriving at Borneo in phase 6 wherein the propagation slows down and later dissipates near New Guinea. While traveling across the Indian Ocean, a portion of rainfall anomalies moves northward toward the Arabian Sea, the Bay of Bengal, and the South China Sea. This northward propagation is accompanied by off-equator Rossby wave response to its northwestern quadrant. The northward ISO decays over the northern plain of India and later over the East China Sea. After 2 or 3 pentads since their arrival at Maritime Continent, rainfall anomalies revive over the western North Pacific (phase 3) and move northwestward toward Taiwan where the previous northward branches still exist. It thus results in an intraseasonally fluctuating rain band along the location of the mean monsoon trough extending from Bay of Bengal, passing through the Indo-China peninsula and South China Sea to the east of Philippine Islands (phase 4). Interacting with the SSTA built up from previous surface flux changes, rainfall anomalies flare up in the tropical eastern Pacific (phase 5).

Both the IP (Figure 10b) and IO (Figure 10d) Runs reasonably reproduce the northward propagating rainfall anomalies over the Indian Ocean sector. The propagation produced by the IO Run in the South Asian monsoon regions is particularly realistic. In the PO Run (Figure 10c), the northward propagation of convection anomalies is nearly absent. Instead, the action center shifts to the western North Pacific. The associated convection/circulation anomalies propagate westward from Philippine Sea toward Taiwan and southeastern China. In addition, they are more viable than their counterparts in the IO Run, suggesting the importance of air-sea interactions to establish the propagating characteristics of off-equator moist Rossby wave. The facts that PO Run has the warmest SSTs over the WNP region in the mean summer climatology (not shown) and rainfall anomalies dissipate rapidly after encountering the land area also point out the considerable contributions of intraseasonal SST variability (0.2℃-0.3℃) that feed back to atmospheric convection (not shown; but refers to Fig. 11b). Interestingly, the ISO over the western North Pacific and East Asia are much stronger than in the IP Run. The Indian Ocean coupling in the IP Run seems to help reduce the amplitude of the unrealistically off-equatorial ISO. It is likely that the northward-propagating ISO originated from the Indian Ocean offset the westward ISO over the western North Pacific and East Asia, or vice versa. It is noted in the observations and the IP and IO Runs that the anomalies in the western North Pacific has an opposite polarity from those in the eastern Indian Ocean. When both the Pacific and Indian Ocean couplings are included, the IP Run produce weaker and more realistic ISO variability in the western North Pacific than the PO Run.

Figure 11 shows the SSTA and surface wind stress anomalies in the observations and the IP Run. Centers of enhanced rainfall in Figure 10 are labeled as open triangles here. In observation (Figure 11a), the positive SSTA show a northward moving tendency which appears first in the Arabian Sea and subsequently in the Bay of Bengal, South China Sea, and northern West Pacific Ocean. The northward ropagating SSTA exhibit a northwest-to-southeast tilting pattern. The enhanced rainfall is preceeded by positive SSTA to the north and followed by negative SSTA to the south, suggesting that the couplings in the Indian Ocean help the summertime ISO propagate northward. The IP Run (Figure 11b) reasonably simulates this northward propagating SSTA over the Arabian Sea and Bay of Bengal. Evolution of the SSTA in the IO Run (not shown) is similar to that in the IP Run. The magnitude of the simulated SSTA extremes (0.3℃~0.5℃) in the IP Run is noticeably comparable with the observation. This is in contrast with its wintertime counterpart where the coupled runs tend to underestimate the magnitude of SSTA (c.f., Figure 7). Similar tendency also occurs in the rainfall anomalies with the simulated magnitude more realistic in MJJASO than in NDJFMA period (c.f., Figure 10 vs. Figure 6). A primary model deficiency in simulating the ISO-related SSTA is the nearly absence of observed eastward component travelling in the low latitudes.

We further examine in Figure 12 the composite LHF and SWR anomalies from the observations and the IP Run. In observations (Figure 12a), a well-organized pattern of positive/negative SWR anomalies (contour lines) with a significant northwest-to-southeast tilting is found to lead the positive/negative SSTA centers [marked by +/－ symbols] about 1/4 cycles. Since the positive/negative SSTA also leads the regions of enhanced/suppressed rainfall anomalies about 1/4 cycles (c.f., Figure 11a), the SWR anomalies, with an opposite sign, thus nearly coincide with the rainfall anomalies due to the changes of cloudiness. In response to the decreased (increased) southwesterly mean flow, which is in turn caused by the suppressed (enhanced) rainfall to the north, the development of the positive (negative) LHF anomalies (colored shading) first appearing in the equatorial western Indian Ocean thus slightly lags that of the positive (negative) SWR anomalies. Nevertheless, with a same polarity, subsequent development of the LHF anomalies eventually catches the ‘saturated’ SWR anomalies while migrating northward towards the latitudes of the Arabian Sea, Bay of Bengal, and southern South China Sea. It is in these regions that the SSTA maxima appear after 1-to-2 pentads. Constrating to the anomalous SWR pattern, which is more or less confined to the eastern hemisphere, a wavenumber 1 (or

2) LHF signal that propagates eastward along the equatorial latitudes can be recognized in both hemispheres as its main body migrates northward. It indicates that the observed planetary-scale feature of the boreal summer ISO is attributed to the underlying LHF that provides the energy source to support the perturbations growing in the free atmosphere aloft.

Like its wintertime counterpart, the largest bias in model still appears in the SWR. It is less organized and magnitude is significantly samller than the LHF in most areas. However, relative phasings between the SWR and LHF anomalies, and their relationships with the SST and rainfall anomalies indeed show some resemblances with the observations. The similarity includes the planetary-scale feature in the LHF anomalies captured by the IP Run. In contrast, the LHF anomalies in both the IO and PO Run (not shown) largely decrease in the respected ocean basin that lacks of the air-sea coupling. Other salient features in the simulation are also noticed. In particular, the development of the northward branch of positive (negative) SWR anomalies initiated along the East African coasts is not intensive enough to offset the predominant negative (positive) LHF anomalies developing in its northeast. This can be identified in both the IP and IO Runs but not in the PO Run where the associated LHF anomalies show no propagation. As a result, the northward moving SSTA in the Arabian Sea is also largely attribued to the local wind-evaporation feedback rather than the cloud-radiation feedback.

Recent studies have suggested that the northward propagation of ISO in the Indian Ocean may be an unstable mode of internal atmospheric dynamics associated with the asymmetric monsoonal flow in boreal summer (Jiang and Li 2005;

Wang 2005). In those studies, the existence of an off-equator EVS basic state provides an intrinsic mechanism for the ISO to propagate northward. The atmosphere-ocean coupling only plays a secondary role to enhance its intensity and set the pace with a more realistic propagation speed. According to the internal dynamic viewpoint, the mean monsoonal circulation determines the extent of the meridional propagation of summertime ISO. To examine this mechanism further, we show in Figure 13 the horizontal distributions of mean EVS in the observation and three model experiments. Here the EVS serves as an index to measure the strength of the summer monsoon, similar to the monsoon circulation index defined by Webster and Yang (1992). The larger the negative values, the stronger the summer monsoon.

In the observation (Figure 13a), negative EVS values extend from the Arabian Sea, the Bay of Bengal, to the South China Sea, coincide reasonably with the regions where the northward ISO propagations are observed (c.f. Figure 10a). The northernmost extent of the ISO propagation also appears to be limited by the boundary of the zero EVS value (near 25°N). Among all the three runs, the PO Run (Figure 13c) produces the most realistic EVS pattern whose extreme values cover a wider meridional extent than both the IP (Figure 13b) and IO (Figure 13d) Runs. This indicates that the PO Run produces a more realistic Asian summer monsoon circulation, probably because its Indian Ocean SSTs are prescribed with the observations. However, the PO Run does not produce a significant ISO propagating northward. Furthermore, the northward propagations in the IP and IO Runs are not limited by their corresponding negative EVS domains. Therefore our basin-coupling results suggest that the northward propagating ISO cannot be explained solely as a result of the atmospheric internal dynamics. Instead, the air-sea coupling in the Indian Ocean constitutes an essential component of the summertime ISO dynamics.

5. Roles of air-sea coupling and monsoon mean flow

We further contrast the ISO simulations produced by the basin-coupling runs with those from the forced AGCM runs. Monthly SST climatologies produced by the coupled runs are used as boundary conditions in the respected coupled ocean basins to drive the same AGCM in an uncoupled configuration. Outside the forced ocean domains, SSTs are still prescribed by the observed monthly-mean climatology. All AGCM runs are integrated for about 13 years, and the last 10 years of the simulations are analyzed. It is noticed in Figure 2 that the variability of filtered U'_{850} (within the 10-to-90-day frequency band) in the forced runs (colored dashed lines) are somewhat larger than those in their corresponding coupled runs (colored solid lines). However, a large portion of it is not associated with the propagating ISO sought in this study. This is verified by the EEOF analysis which shows that the variability of EVS in the forced runs tends to spread over into higher order modes rather than being dominated by the leading mode as in the coupled runs and observation.

The EEOF analysis and composite procedure are applied to the AGCM runs to construct the lifecycle of the simulated ISO. The upper panels in Figure 14 show the evolutions of the wintertime χ'_{200} along the equator (averaged between 10°S and 10°N). It is found that the extreme values of χ'_{200} simulated by the AGCM runs are about 15-25% smaller than those in their corresponding CGCM runs (see Figure 4). Most importantly, the eastward propagating feature seen in the coupled runs is interrupted and replaced by a strong standing feature in the AGCM runs. Standing oscillation is particularly evident in the forced IO Run (Figure 14c), suggesting a crucial role of the coupling in the Indian Ocean and Maritime Continent to the eastward propagating ISO in boreal winter.

In boreal summer, the χ'_{200} produced by the AGCM runs (lower panels in Figure 14) also shows weaker intensities and stronger standing features than their counterparts in the CGCM runs (in Figure 9). It is then noticed that the differences in magnitude between the forced and coupled runs are less obvious than those in the wintertime comparisons. Interestingly, the eastward propagating feature over the Indian Ocean sector (60°E-to-120°E) shown in the coupled IP (Figure 9b) and IO (Figure 9d) Runs still stands out in the AGCM runs (Figure 14d, f). This is different from its wintertime counterpart, in which the simulated ISO changes from propagating to standing when the Indian Ocean coupling is turned off (i.e. from coupled to forced runs). This suggests that the atmospheric internal dynamics may play an important role in affecting the propagation of ISO in summertime.

Figure 15 shows the evolutions of U'_{850} (contour lines) superimposed on the rainfall (colored shading) composites for both the coupled and forced GCM experiments in boreal winter. For our reference, the observation is also shown (Figure 15a). Contrasting the forced runs (lower panels) with their coupled counterparts (upper panels), the decreased magnitudes and erroneous standing components stand out in both anomalous fields while lacking of the coupling. Actually, the propagation feature of rainfall anomalies cannot be identified at all, demonstrating the crucial role of air-sea coupling for the ISO-related rainfall to propagate eastward. We then notice that the decreased magnitude in the extremes of U'_{850} is around 20~25% in the forced IO Run (panel d vs. g), but it can reach 35~50% in the forced PO Run (panel c vs. f). Indication pointing to the importance of Pacific Ocean coupling is reinforced by the fact that the propagating component of the U'_{850} is absent in the forced PO Run (panel f). Conclusively, model's capability in passing through the Maritime Continent (105°E~120°E; see panel a) and thus allowing the rainfall anomalies to propagate eastward into the western Pacific is attributed to an interactive Pacific Ocean.

To highlight the relative roles between the air-sea coupling and atmospheric internal dynamics upon the northward propagating ISO in boreal summer, we show in Figure 16 the time-latitude plots of the U'_{850} and rainfall composites in various experiments around the longitudes of Bay of Bengal (averaged between 85°E and 95°E). Some salient features are as follows. Firstly, like the wintertime ISO, lacking of the coupling not only results in the decrease of anomalous magnitude but also the absence of propagating feature in the ISO-related convection (panel b vs. d, and panel c vs. e), consistent with the finding in some recent studies (e.g., Fu and Wang 2004). Secondly, the evolution of U'_{850} somewhat still owes a northward propagating signal even if the Indian Ocean coupling is absent (panel e), suggesting the increased role of atmospheric internal dynamics to aid the ISO propagation when an asymmetric monsoonal circulation appears in boreal summer (Wang and Xie 1997). Finally, when the air-sea coupling is excluded in the forced IP Run (panel d), the northernmost latitude (around 15°N; vertical green line) that the dwindling zonal winds' propagation can reach coincides with the northern boundary of seasonal-mean negative EVS (c.f., Figure 13b). However, it is not the case in the corresponding coupled run (panel b) that allows the simulated U'_{850} to cross the northern boundary of seasonal-mean negative EVS and thus leads to a latitudinal extent closer to the observation. Although it could be model dependent, it leads us to conclude that the Indian Ocean coupling plays an essential rather than a secondary role for the northward propagation of ISO in boreal summer.

6. Summary and conclusions

In this study, we demonstrated with three basin-coupling CGCM experiments that the couplings in the Pacific and Indian oceans play different roles to the ISO between boreal winter and boreal summer. We found that the Pacific Ocean coupling is important to sustain the eastward propagation of the wintertime ISO and the Indian Ocean coupling is crucial to the meridional propagation of summertime ISO.

In boreal winter, when the warm SSTs locate mostly zonally along the equator and extend from the Indian Ocean to the central Pacific, the ISO propagation is primarily eastward, and the Pacific Ocean coupling is important for ISO to propagate eastward into the western Pacific. When the Pacific Ocean coupling is included, both the IP and PO Runs produce a realistic eastward propagation, even though these two runs have biases in their simulated SSTs. Without the Pacific Ocean coupling, the ISO in the IO Run cannot maintain its eastward voyage but bifurcates toward the mid-latitudes of both hemispheres while approaching the Maritime Continent. The basin-coupling experiments further show that the extent of low-level mean westerlies near the Maritime Continent conditions the present CGCMs to have a realistsic ISO simulation (e.g., Inness and Slingo 2003, Zhang et al. 2006, Watterson and Syktus 2007). Such wind biases can be further linked to the mean SST biases that are responsible for the erroneous standing oscillations found in the central Indian Ocean (near 60 °E) and the central Pacific Ocean (180°E).

In boreal summer, when the warm SSTs retract westward and shift into the Northern Hemisphere, the northward propagating component enhances while its eastward propagating component weakens. In this season, most of the propagations occur in the northern Indian Ocean and the western North Pacific. This allows the Indian Ocean coupling to become important to the ISO propagation. The IO Run produces the most realistic simulation of the northward ISO propagation, while the PO Run fails to simulate the northward propagation.

Results of the composite analyses in both seasons showed that the air-sea couplings promote the ISO propagations by configuring a proper temporal and spatial phase relationship between the surface fluxes, winds, convection, and underlying SST fluctuations. In this particular CGCM, however, the ISO-SST interaction is produced mainly via latent heat flux through the wind-evaporation feedback. In the observations the interaction is also produced via short wave radiation flux through the convection-cloud feedback. From the forced AGCM experiments, we found that no ISO propagation exists once the ocean couplings are turned off.

The relative roles between the air-sea coupling in the Indian Ocean and the off-equator monsoon mean flow in shaping the summertime ISO's northward propagation are further examined by comparing the coupled runs with their forced versions. Results indicate that 1) the northward propagating feature in the ISO-related convection exists only when an interactive Indian Ocean is included; 2) the atmospheric internal dynamics aiding the propagating feature of ISO is recognized mainly in the associated dynamic aspect of low-level zonal winds though with the significantly reduced magnitude when the coupling is excluded; 3) Indian Ocean coupling helps the simulated ISO to cross the northern boundary of mean negative EVS, resulting in a more realistic simulation. It therefore concludes that the coupling plays an essential rather than a secondary role for simulating the northward propagating ISO.

Acknowledgments The authors wish to thank Dr. Ian G. Watterson, Dr. Chidong Zhang, and one anonymous reviewer for their valuable comments and suggestions on the original manuscript. The authors express their gratitude to Mr. Wen-Haung Huang who helped to prepare the figures. SPW was supported by the National Science Council of Taiwan under Grants NSC94-2119-M-003-004 and NSC95-2111-M-003-002. JYY was supported by the National Science Foundation of USA under Grant ATM-0638432.

REFERENCES

Bhat GS et al (2001) BOBMEX−The Bay of Bengal Monsoon Experiment. Bull Amer Meteor Soc 82(10):2217–2243

Bryan K (1969) A numerical method for the study of the circulation of the world ocean. J Comp Phys 4:347–376

Cox MD (1984) A primitive equation three-dimensional model of the ocean. GFDL Ocean Group Tech Rep No1 75 pp

Cubukcu N, Krishnamurti TN (2002) Low-frequency controls on the thresholds of sea surface temperature over the western tropical Pacific. J Clim 15(13):1626-1642

Fu X, Wang B (2004) Differences of boreal-summer intraseasonal oscillations simulated in an atmosphere-ocean coupled model and an atmosphere-only model. J Clim 17(6):1263-1271

Gualdi S, Navarra A, Fischer M (1999) The tropical intraseasonal oscillation in a coupled ocean-atmosphere general circulation model. Geophy Res Lett 26:2973-2976

Hendon HH (2000) Impact of air–sea coupling on the Madden–Julian oscillation in a general circulation model. J Atmos Science 57(24):3939–3952

Hendon HH, Glick J (1997) Intraseasonal air–sea interaction in the tropical Indian and Pacific Oceans. J Clim 10(4):647–661

Hendon HH, Salby ML (1994) The life cycle of the Madden–Julian oscillation. J Atmos Sci 51(15):2225–2237

Hsu HH, Weng CH (2001) Northwestward propagation of the intraseasonal oscillation in the western north Pacific during the boreal summer: Structure and mechanism. J Clim 14(18):3834-3850

Hsu HH, Weng CH, Wu CH (2004) Contrasting characteristics between the northward and eastward propagation of the intraseasonal oscillation during the boreal summer. J Clim 17(4):727-743

Inness PM, Slingo JM (2003) Simulation of the Madden–Julian oscillation in a coupled general circulation model. Part I: Comparison with observations and an atmosphere-only GCM. J Clim 16(3):345–364

Jiang X, Li T (2005) Reinitiation of the boreal summer intraseasonal oscillation in the tropical Indian Ocean. J Clim 18(18):3777–3795

Jones C, Carvalho LMV, Higgins RW, Waliser DE, Schemm JKE (2004) Climatology of tropical intraseasonal convective anomalies 1979–2004. J Clim 17(3):523–539

Kemball-Cook SR, Wang B (2001) Equatorial waves and air-sea interaction in the boreal summer intraseasonal oscillation. J Clim 14(13):2923-2942

Krishnamurti TN, Osterhof DK, Mehta AV (1988) Air–sea interaction on the time scale of 30–50 days. J Atmos Science 45(8):1304–1322

Krishnamurti TN, Subrahmanyam D (1982) The 30-50 day mode at 850 mb during MONEX. J Atmos Science 39(9):2088-2095

Lau KM, Sui CH (1997) Mechanisms for short-term sea surface temperature regulation: Observations during TOGA COARE. J Clim 10(3):465–472

Lau KM, Chan PH (1986) Aspects of the 40-50 day oscillation during the northern summer as inferred from outgoing longwave radiation. Mon Weather Rev 114(7):1354-1367

Liu P, Wang B, Sperber KR, Li T, Meehl GA (2005) MJO in the NCAR CAM2 with the Tiedtke convective scheme. J Clim 18(15):3007-3020

Madden RA, Julian PR (1971) Detection of a 40-50 day oscillation in the zonal wind in the tropical Pacific. J Atmos Science 28(5):702-708

Madden RA, Julian PR (1972) Description of global-scale circulation cells in the tropics with a 40-50 day period. J Atmos Science 29(6):1109-1123

Maloney ED (2002) An intraseasonal oscillation composite life cycle in the NCAR CCM3.6 with modified convection. J Clim 15(9):964–982

Mechoso CR et al (1995) The seasonal cycle over the tropical Pacific in general circulation models. Mon Weather Rev 123(9):2825-2838

Mechoso CR, Yu JY, Arakawa A (2000) A coupled GCM pilgrimage: From climate catastrophe to ENSO simulations. In: D. A. Randall (editor), *General Circulation Model Development: Past, Present, and Future*, Academic Press, London 539–575

Reynolds RW, Rayner NA, Smith TM, Stokes DC, Wang W (2002) An improved in situ and satellite SST analysis for climate. J Clim 15(13):1609–1625

Rui H, Wang B (1990) Development characteristics and dynamic structure of tropical intraseasonal convection anomalies. J Atmos Science 47(3):357–379

Uppala SM et al (2005) The ERA-40 re-analysis. Q J Roy Meteor Soc 131(612):2961-3012 doi:10.1256/qj.04.176

Waliser DE, Lau KM, Kim JH (1999) The influence of coupled SSTs on the Madden–Julian oscillation: A model perturbation experiment. J Atmos Science 56(3):333–358

Wang B (2005) Theory. In: William K.-M. Lau and D. E. Waliser (editors), *Tropical Intraseasonal Oscillation in the Atmosphere and Ocean*. Praxis Publishing Ltd, Chichester, UK, 307-360

Wang B, Rui H (1990) Synoptic climatology of transient tropical intraseasonal convection anomalies. Meteor Atmos Phys 44(1-4):43-61

Wang B, Xie X (1997) A model for the boreal summer intraseasonal oscillation. J Atmos Science 54(1):72-86

Wang B, Xie X (1998) Coupled modes of the warm pool climate system Part I: The role of air-sea interaction in maintaining Madden-Julian oscillation. J Clim 11(8): 2116-2135

Wang B, Fan Z (1999) Choice of South Asian summer monsoon indices. Bull Amer Meteor Soc 80(4):629-638

Watterson IG (2002) The sensitivity of subannual and intraseasonal tropical variability to model ocean mixed layer depth. J Geophys Res 107. DOI 10.1029/2001JD000671

Watterson IG, Syktus J (2007) The influence of air-sea interaction on the Madden-Julian Oscillation: the role of seasonal mean state. Clim Dyn 28. DOI 10.1007/s00382-006-0206-9

Weare BC, Nasstrom JS (1982) Examples of extended empirical orthogonal functions. Mon Weather Rev 110(6):481-485

Webster PJ et al (2002) The JASMINE pilot study. Bull Amer Meteor Soc 83(11):1603–1630

Webster PJ, Yang S (1992) Monsoon and ENSO: Selectively interactive systems. Q J Roy Meteor Soc 118(507):877-926

Weller RA, Anderson SP (1996) Surface meteorology and air-sea fluxes in the western equatorial Pacific warm pool during the TOGA coupled ocean-atmosphere response experiment. J Clim 9(8):1959-1990

Wheeler MC, Hendon HH (2004) An all-season real-time multivariate MJO index: Development of an index for monitoring and prediction. Mon Weather Rev 132(8): 1917-1932

Woolnough SJ, Slingo JM, Hoskins BJ (2000) The relationship between convection and sea surface temperature on intraseasonal timescales. J Clim 13(12):2086–2104

Wu MLC, Schubert A, Kang IS, Waliser D (2002) Forced and free intraseasonal variability over the South Asian monsoon region simulated by 10 AGCMs. J Clim 15(20):2862–2880

Xie P, Arkin PA (1997) Global precipitation: A 17-year monthly analysis based on gauge observations, satellite estimates, and numerical model outputs. Bull Amer Meteor Soc 78(11):2539 - 2558

Yasunari T (1980) A quasi-stationary appearance of 30- to 40-day period in the cloudiness fluctuations during the summer monsoon over India. J Meteor Soc Jpn 58:225-229

Yasunari T (1981) Structure of an Indian monsoon system with around 40-day period. J Meteor Soc Jpn 59:336-354

Yu JY, Mechoso CR (2001) A coupled atmosphere–ocean GCM study of the ENSO cycle. J Clim 14(10):2329–2350

Zhang C (1996) Atmospheric intraseasonal variability at the surface in the tropical western Pacific Ocean. J Atmos Science 53(5):739-758

Zhang C (1997) Intraseasonal variability of the upper-ocean thermal structure observed at 0° and 165°E. J Clim 10(12):3077-3092

Zhang C, Dong M, Gualdi S, Hendon HH, Maloney ED, Marshall A, Sperber KR, Wang W (2006) Simulations of the Madden-Julian oscillation in four pairs of coupled and uncoupled global models. Clim Dyn 27(6):573-592. DOI 10.1007/s00382-006-0148-22

Zhang C, McPhaden MJ (2000) Intraseasonal surface cooling in the equatorial west Pacific. J Clim 13(13):2261-2276

Figure captions

Fig. 1 The observed SST climatology in boreal (a) winter (November-April; NDJFMA) and (b) summer (May-October; MJJASO) based on NOAA OISST_v2 dataset (1981-2001 averaged). The 30-yr SST climatology simulated by the Indo-Pacific (IP) Run is shown in (c) for NDJFMA and in (d) for MJJASO period, respectively. Contour interval is 1°C, and areas of mean SST value larger than (27°, 28°, 29°)C are (gray, dark, black) shaded.

Fig. 2 The longitudinal distribution of standard deviation of the U'_{850} variance along the equator (averaged between 10°S and 10°N) in (a) NDJFMA and (b) MJJASO for the observation (ERA40, in black), 3 coupled runs (colored solid lines), and corresponding forced experiments (colored dashed lines) using the SST product generated by the coupled runs.

Fig. 3 The evolutions of the first EEOF mode in the observed easterly vertical shear (EVS) anomalies. Only one half of it between phase 1 (-25 days) and phase 6 (+0 day) are shown in the left panels for NDJFMA and in the right panels for MJJASO. The positive and negative EVS eigenvectors are contoured in solid and dashed lines, respectively.

Fig. 4 The Hovmöller diagrams of the composite wintertime ISO life cycle portrayed by the 200mb velocity potential anomalies (χ'_{200}) along the equator (averaged between 10°S and 10°N) for the (a) observation (i.e., ERA40), (b) IP Run, (c)

PO Run, and (d) IO Run. The contour interval of χ'_{200} equals to 1.0 x 10^6 $m^2 \cdot sec^{-1}$ in (a) and 1/3 x 10^6 $m^2 \cdot sec^{-1}$ in (b)-(d).

Fig. 5 (a) The observation (from ERA40), (b) IP Run, (c) PO Run, and (d) IO Run simulated winter-mean (NDJFMA) total winds (vectors) and velocity potential (color-shaded) at 850-mb. The tropical westerlies are highlighted as red vectors.

Fig. 6 The wintertime (NDJFMA) ISO life cycles in the rainfall and 850-mb wind anomalies are shown for (a) observation, (b) IP, (c) PO, and (d) IO Runs. Only the first half of the life cycle from phase 1 (-25 day) to phase 6 (+0 day) are shown. Color-shaded areas and the black vectors denote, respectively, the rainfall and wind anomalies significant at 95% (90%) confidence level. Note that the different scales are used between observed and simulated wind as well as rainfall anomalies.

Fig. 7 The wintertime (NDJFMA) ISO life cycles in the SST (colored shading with contour lines) and surface wind stress (vectors) anomalies are shown for (a) the observation and (b) IP Run. The centers of enhanced rainfall anomalies in Figs. 6a and 6b are labeled as open triangles here. Note that the scale used in simulated SST anomalies is only one half of that used in the observations.

Fig. 8 The wintertime (NDJFMA) ISO life cycles in the anomalous LHF (colored shading) and SWR (contour lines) are shown for (a) the observation and (b) IP Run. The positive (negative) anomalies represent enhanced downward (upward) fluxes. The enhanced rainfall and positive/negative SSTA centers are labeled as open triangles and ＋/－, respectively. Note that the scale used in the simulated anomalies is only one half of that used in the observations. The C.I. of observed (simulated) SWR anomalies is 5 (2.5) W/m^2.

Fig. 9 The configurations are the same as those in Fig. 4, except for the MJJASO period and values of velocity potential are averaged between 14°N and 2°S.

Fig. 10 The summertime (MJJASO) ISO life cycles in the rainfall and 850-mb wind anomalies are shown for (a) observation, (b) IP, (c) PO, and (d) IO Runs. Only the first half of the life cycle from phase 1 (-25 day) to phase 6 (+0 day) are shown. Color-shaded areas and the black vectors denote the rainfall and wind anomalies significant at 95% (90%) confidence level, respectively. Note that the different scales are used between observed and simulated wind anomalies.

Fig. 11 The configurations are the same as those in Fig. 7, except for the MJJASO period. The centers of enhanced rainfall anomalies in Figs. 10a and 10b are marked as open triangles here. Note that the same scale is used for SST anomalies in observation and IP Run.

Fig. 12 The configurations are the same as those in Fig. 8, except for the MJJASO period. Enhanced rainfall (in Fig.10a, b) and positive/negative SSTA (in Fig. 11) centers are marked as open triangles and +/−, respectively. Note that the same scale is used in both observed and simulated anomalies. The contour interval of SWR anomalies is 5.0 W/m^2.

Fig. 13 (a) The observation, (b) IP Run, (c) PO Run, and (d) IO Run simulated mean EVS in MJJASO. Only negative values of EVS are shaded and contoured with 5 m · sec^{-1} intervals.

Fig. 14 The Hovmöller diagrams of the compositing χ'_{200} in the forced experiments of IP [(a) and (d)], PO [(b) and (e)], and IO [(c) and (f)] runs. The upper (lower) 3 panels are for the wintertime (summertime) averaged between 10°S and 10°N (2°S and 14°N). Contour interval is 1/3 x 10^6 m^2 · sec^{-1}.

Fig. 15 The Hovmöller diagrams of the wintertime U'_{850} (contour lines; solid: westerly) and rainfall (color shading) composites in observation (a), 3 coupled runs [(b)-(d)], and 3 forced runs [(e)-(g)]. Anomalies are averaged between 10°S and 10°N. The contour interval of U'_{850} is 1.0 m/sec in panel (a), and 0.5 m/sec elsewhere. Note that the scaling (value inside the parenthesis) used for the simulated rainfall anomalies is only 1/2 of that used for the observations. The straight diagonal lines mark the eastward phase speed around 5 $m \cdot sec^{-1}$.

Fig. 16 The time-latitude diagrams of the summertime U'_{850} (contour lines; solid: westerly) and rainfall (color shading) composites in the (a) observation, (b) IP Run , and (c) IO Run, (d) forced IP Run, and (e) forced IO Run. Anomalies are averaged between 85°E and 95°E in the longitudes around Bay of Bengal. Contour interval of U'_{850} is 1.0 m/sec in panel (a), and 0.5 m/sec elsewhere. Vertical green lines mark the averaged locations of zero contours in the seasonal-mean EVS.

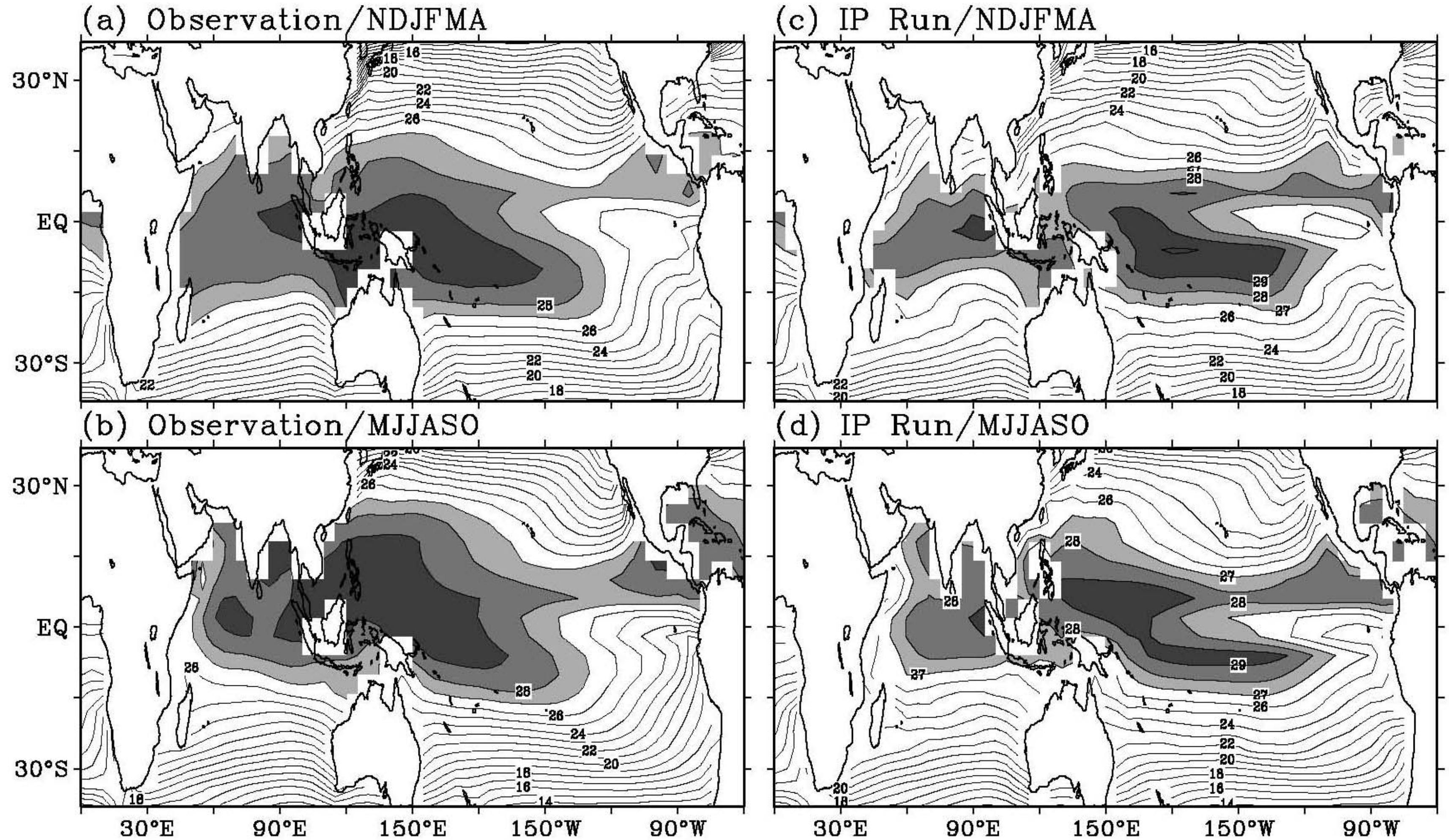

Fig. 1 The observed SST climatology in boreal (a) winter (November-April; NDJFMA) and (b) summer (May-October; MJJASO) based on NOAA OISST_v2 dataset (1981-2001 averaged). The 30-yr SST climatology simulated by the Indo-Pacific (IP) Run is shown in (c) for NDJFMA and in (d) for MJJASO period, respectively. Contour interval is 1°C, and areas of mean SST value larger than (27°, 28°, 29°)C are (gray, dark, black) shaded.

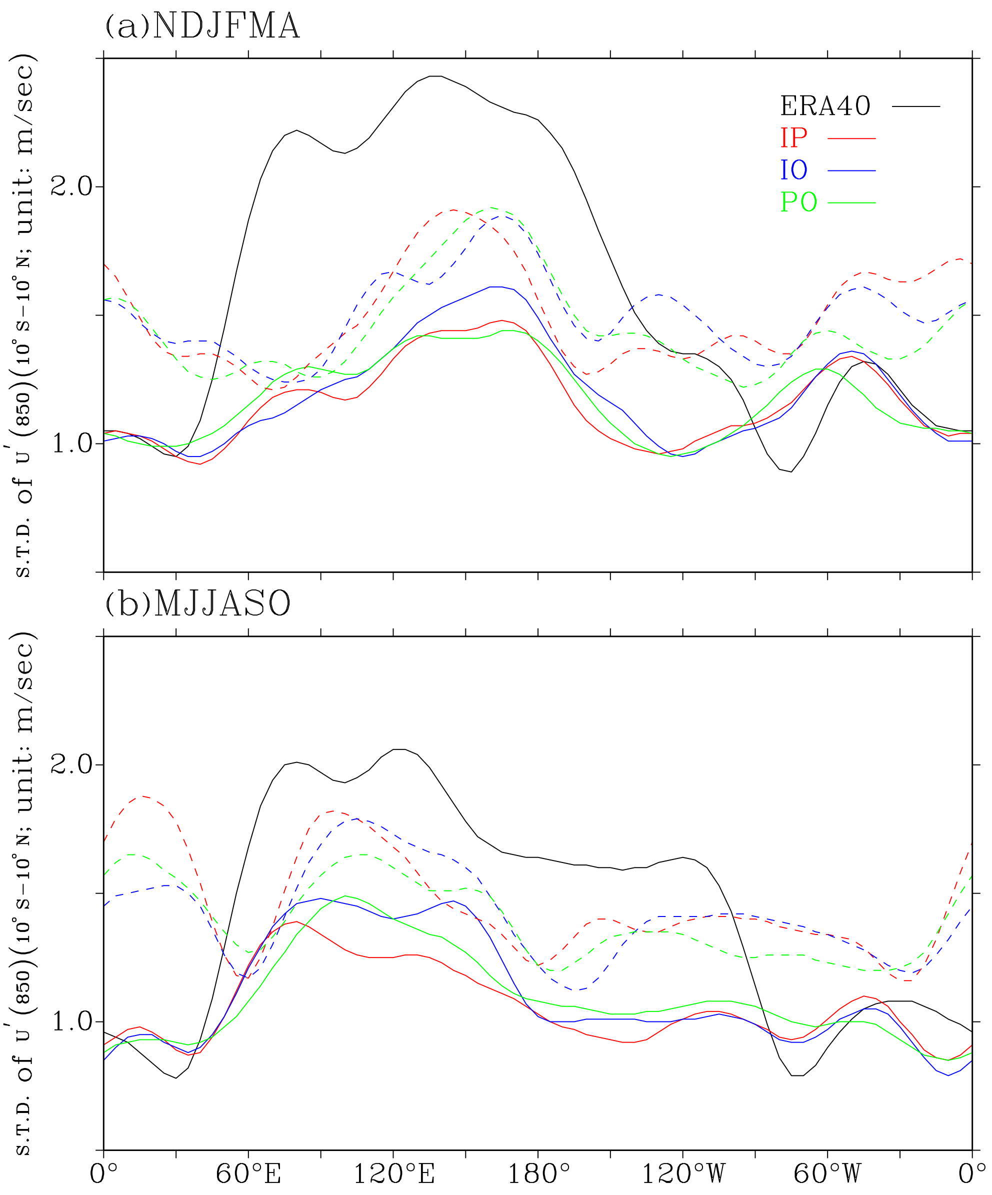

Fig. 2 The longitudinal distribution of standard deviation of the U'_{850} variance along the equator (averaged between 10°S and 10°N) in (a) NDJFMA and (b) MJJASO for the observation (ERA40, in black), 3 coupled runs (colored solid lines), and corresponding forced experiments (colored dashed lines) using the SST product generated by the coupled runs.

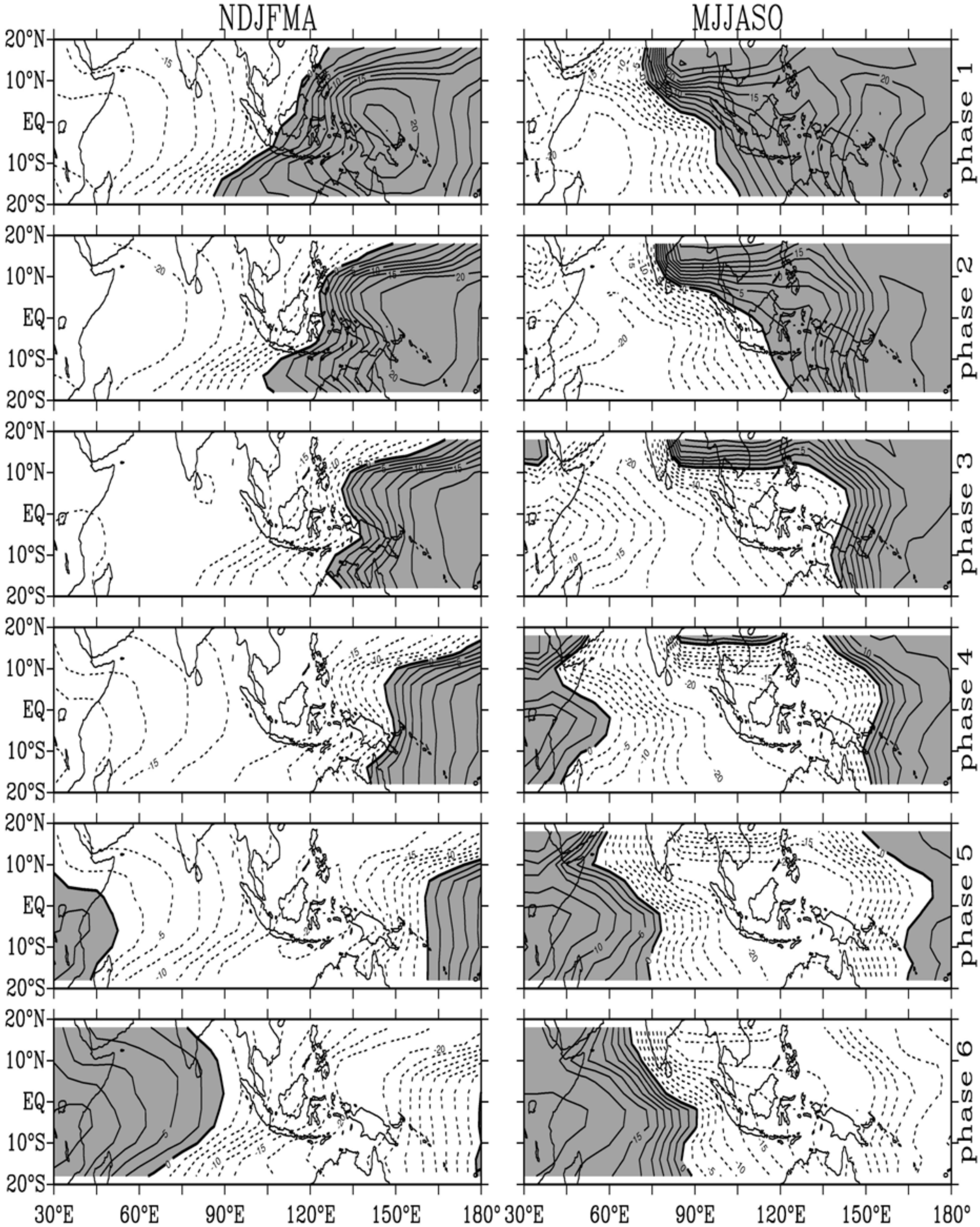

Fig. 3 The evolutions of the first EEOF mode in the observed easterly vertical shear (EVS) anomalies. Only one half of it between phase 1 (-25 days) and phase 6 (+0 day) are shown in the left panels for NDJFMA and in the right panels for MJJASO. The positive and negative EVS eigenvectors are contoured in solid and dashed lines, respectively.

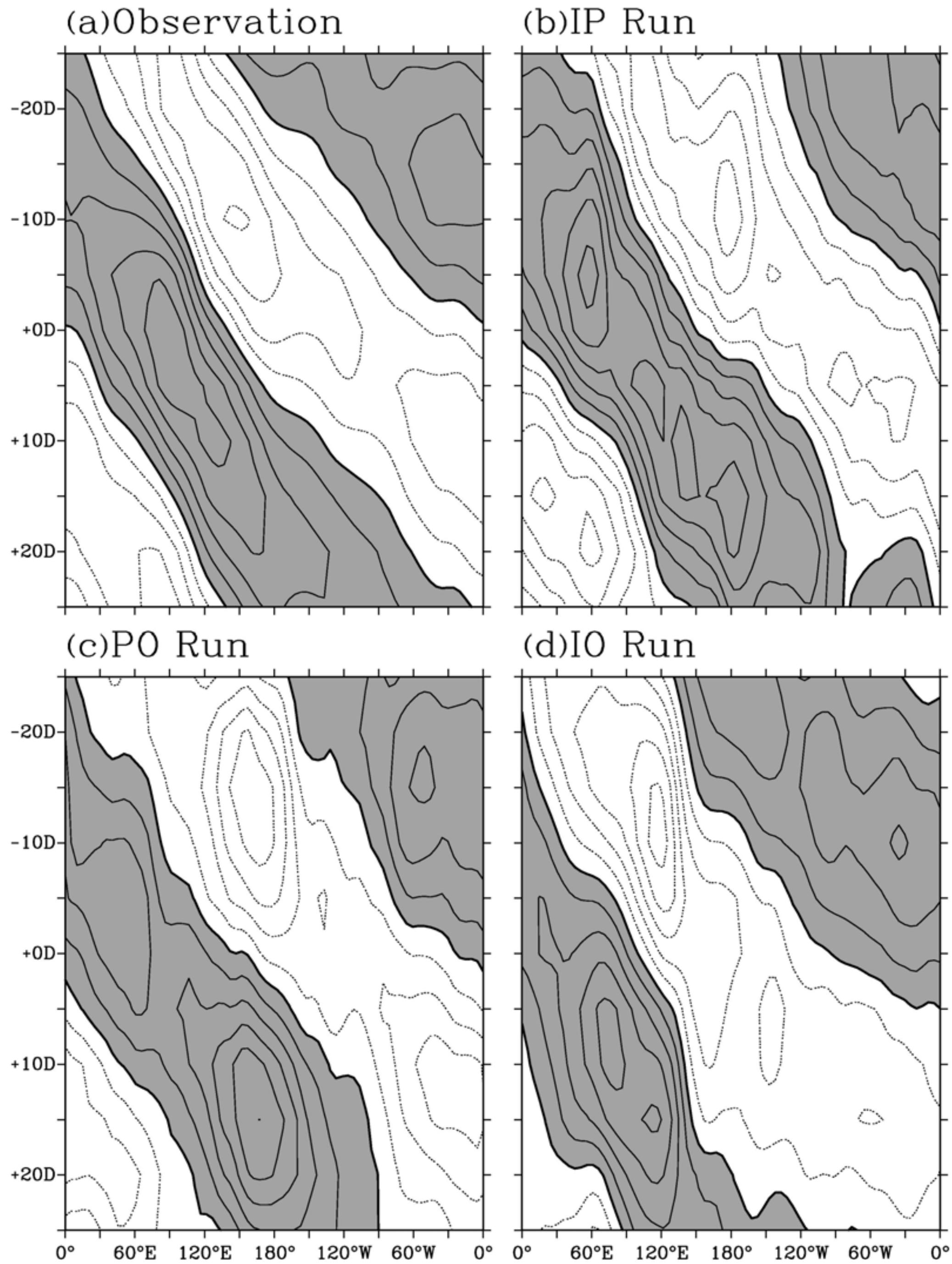

Fig. 4 The Hovmöller diagrams of the composite wintertime ISO life cycle portrayed by the 200mb velocity potential anomalies (χ'_{200}) along the equator (averaged between 10°S and 10°N) for the (a) observation (i.e., ERA40), (b) IP Run, (c) PO Run, and (d) IO Run. The contour interval of χ'_{200} equals to 1.0 x 10^6 $m^2 \cdot sec^{-1}$ in (a) and 1/3 x 10^6 $m^2 \cdot sec^{-1}$ in (b)-(d).

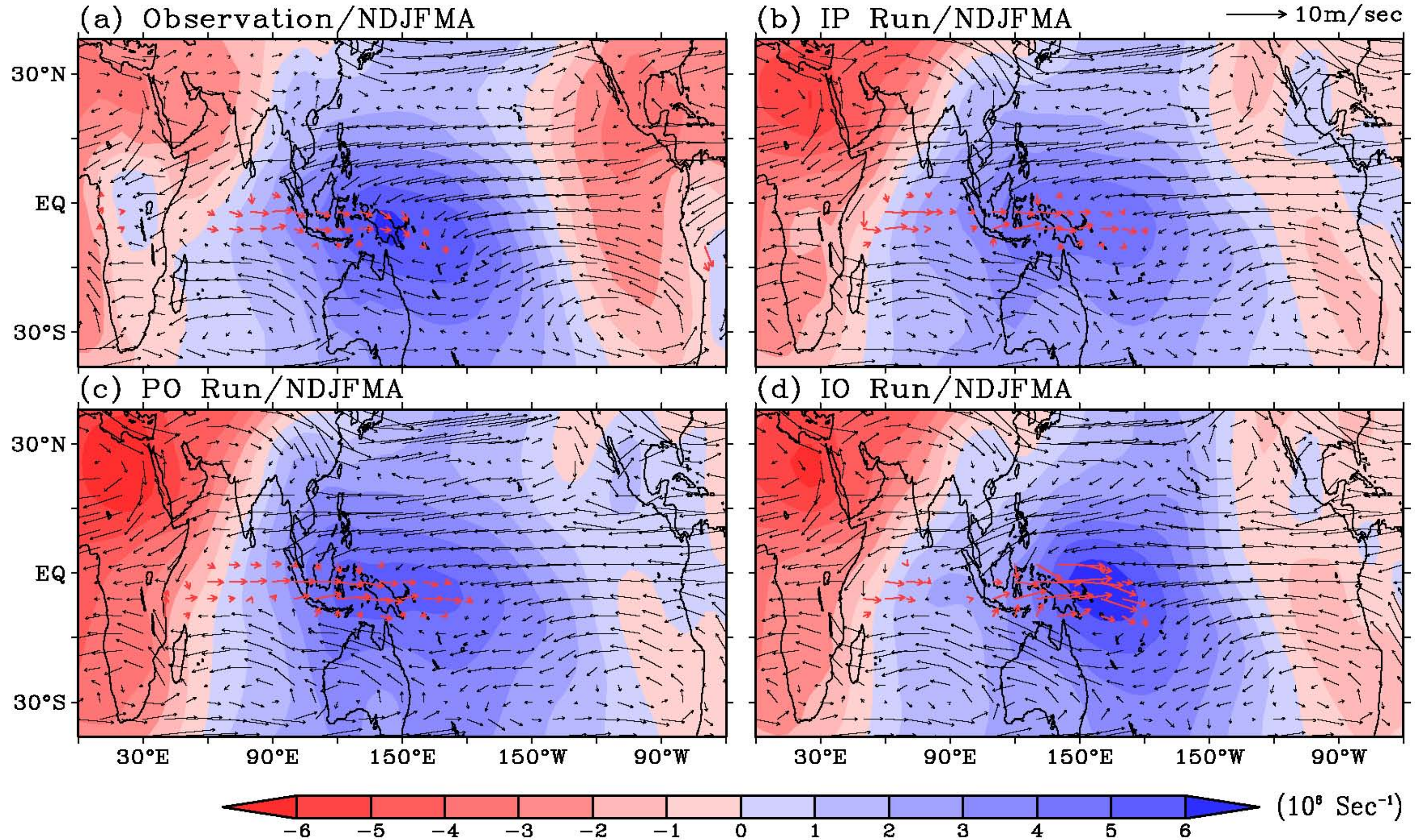

Fig. 5 (a) The observation (from ERA40), (b) IP Run, (c) PO Run, and (d) IO Run simulated winter-mean (NDJFMA) total winds (vectors) and velocity potential (color-shaded) at 850-mb. The tropical westerlies are highlighted as red vectors.

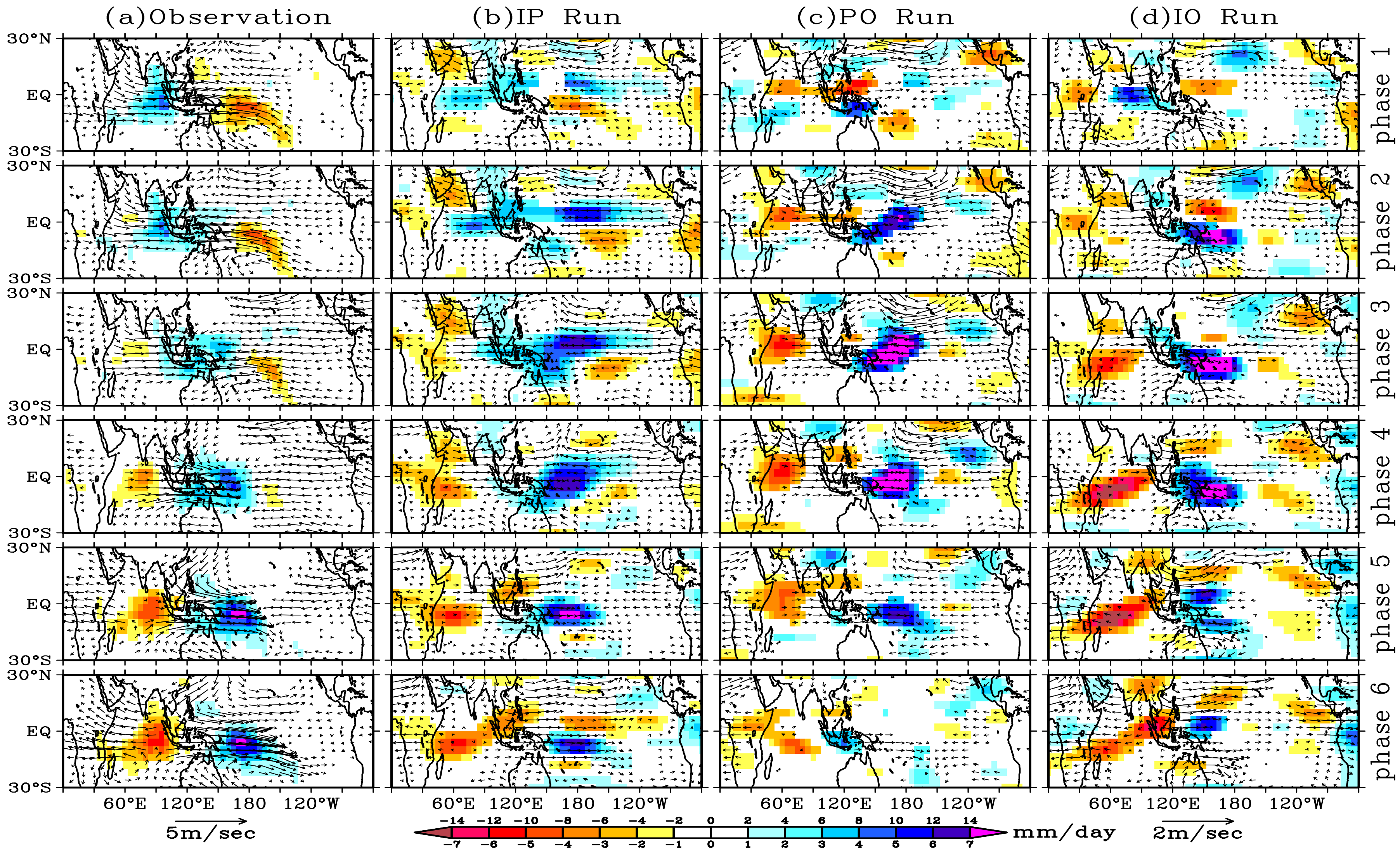

Fig. 6 The wintertime (NDJFMA) ISO life cycles in the rainfall and 850-mb wind anomalies are shown for (a) observation, (b) IP, (c) PO, and (d) IO Runs. Only the first half of the life cycle from phase 1 (-25 day) to phase 6 (+0 day) are shown. Color-shaded areas and the black vectors denote, respectively, the rainfall and wind anomalies significant at 95% (90%) confidence level. Note that the different scales are used between observed and simulated wind as well as rainfall anomalies.

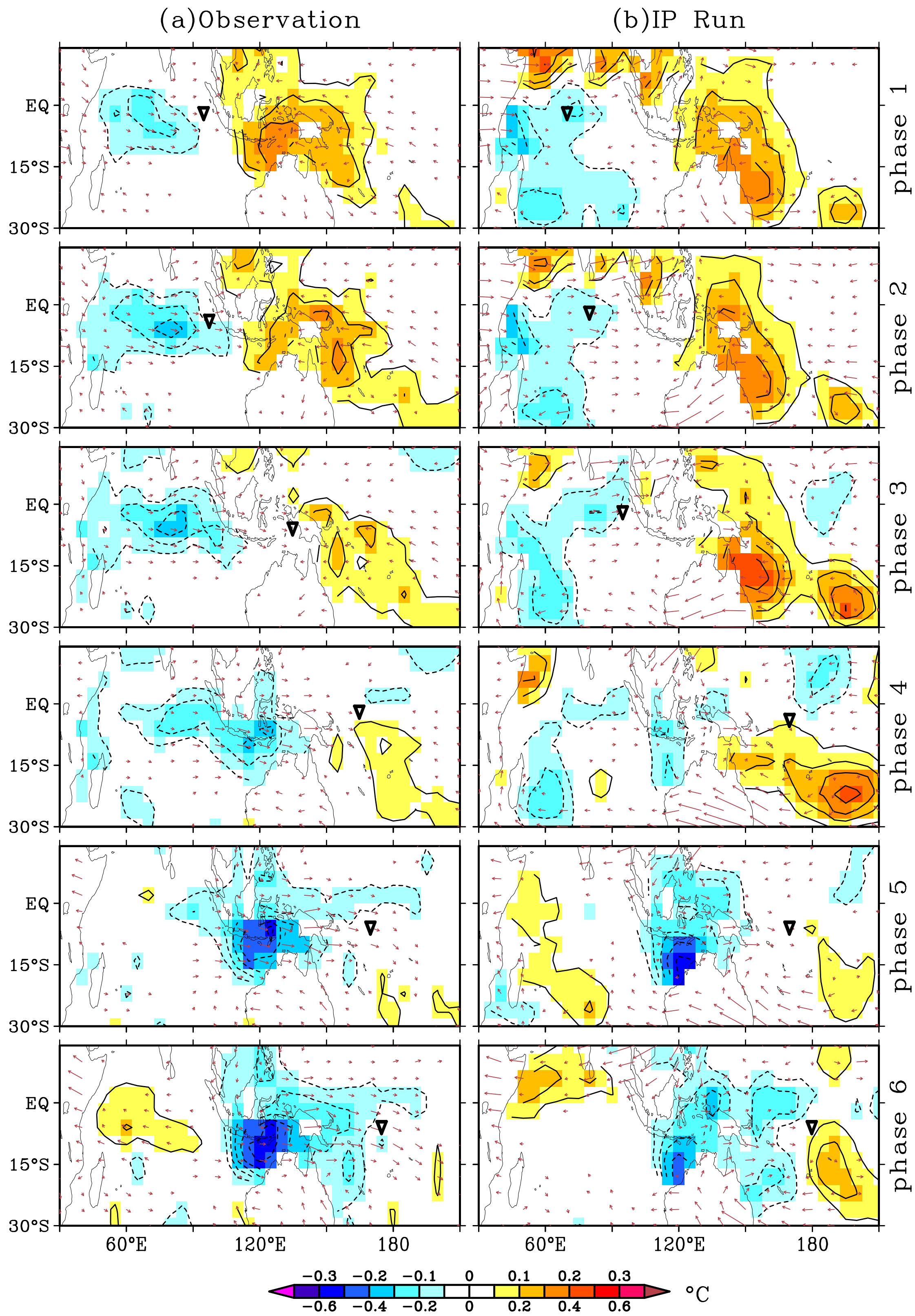

Fig. 7 The wintertime (NDJFMA) ISO life cycles in the SST (colored shading with contour lines) and surface wind stress (vectors) anomalies are shown for (a) the observation and (b) IP Run. The centers of enhanced rainfall anomalies in Figs. 6a and 6b are labeled as open triangles here. Note that the scale used in simulated SST anomalies is only one half of that used in the observations.

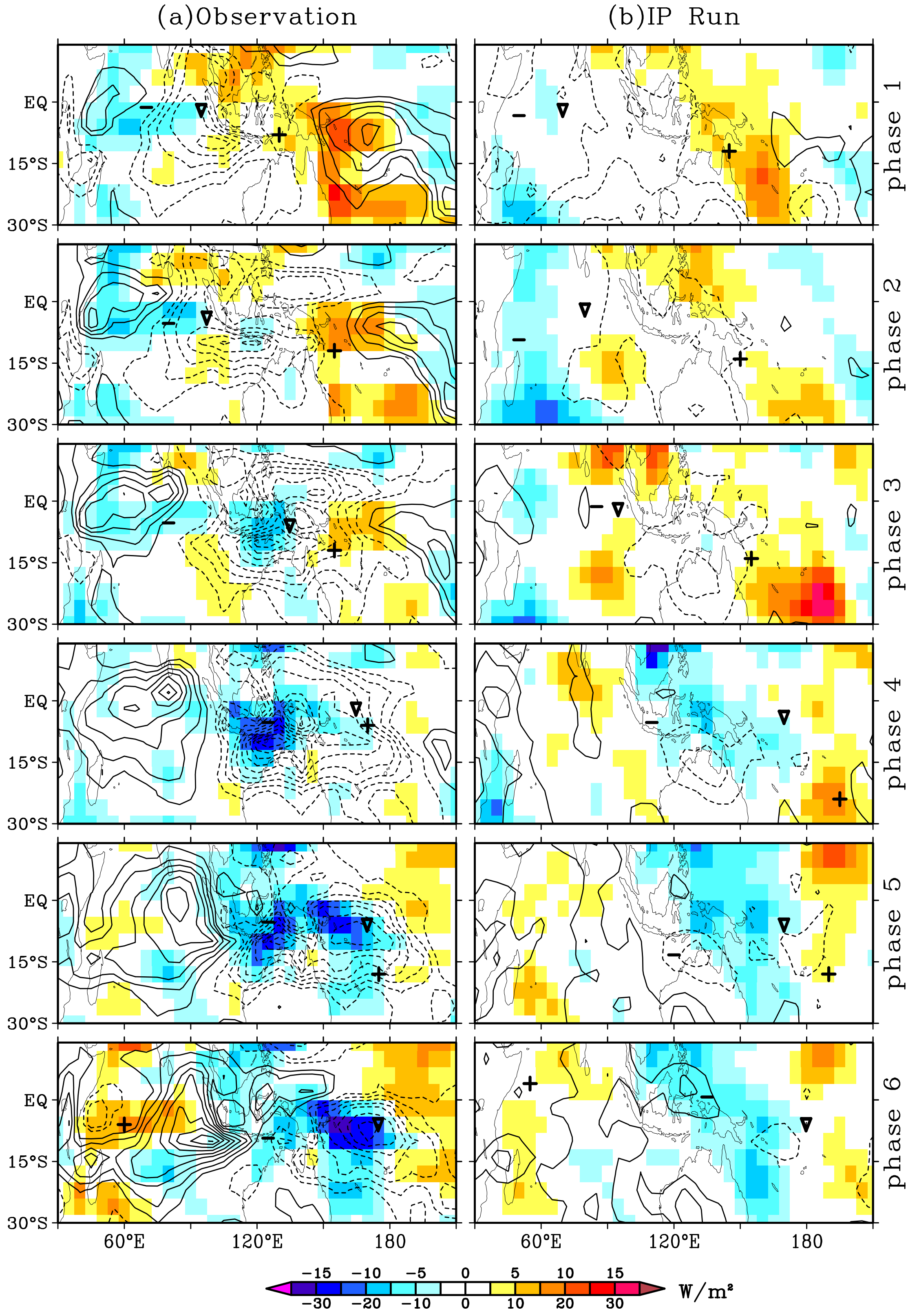

Fig. 8 The wintertime (NDJFMA) ISO life cycles in the anomalous LHF (colored shading) and SWR (contour lines) are shown for (a) the observation and (b) IP Run. The positive (negative) anomalies represent enhanced downward (upward) fluxes. The enhanced rainfall and positive/negative SSTA centers are labeled as open triangles and ＋/—, respectively. Note that the scale used in the simulated anomalies is only one half of that used in the observations. The C.I. of observed (simulated) SWR anomalies is 5 (2.5) W/m^2.

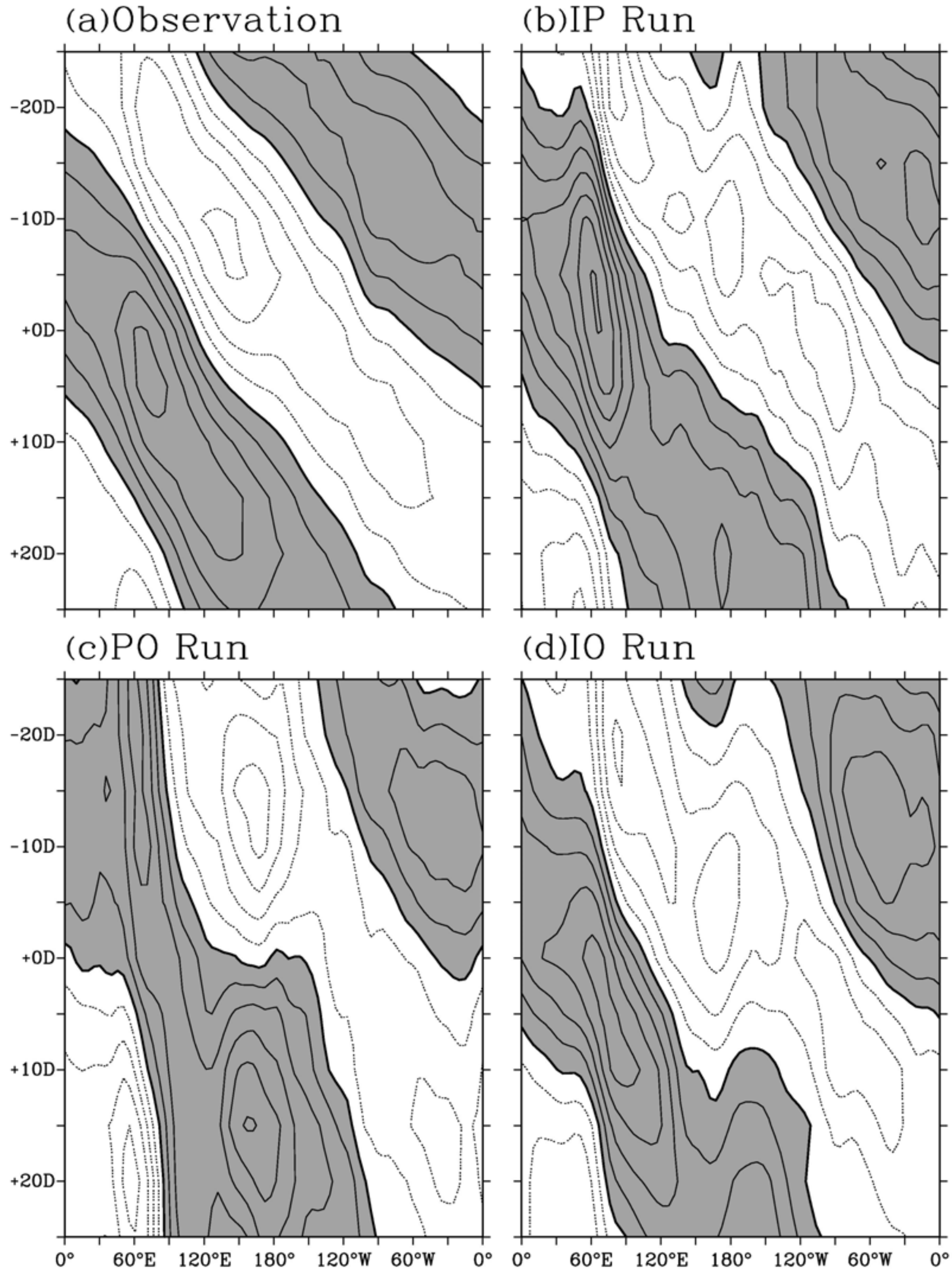

Fig. 9 The configurations are the same as those in Fig. 4, except for the MJJASO period and values of velocity potential are averaged between 14°N and 2°S.

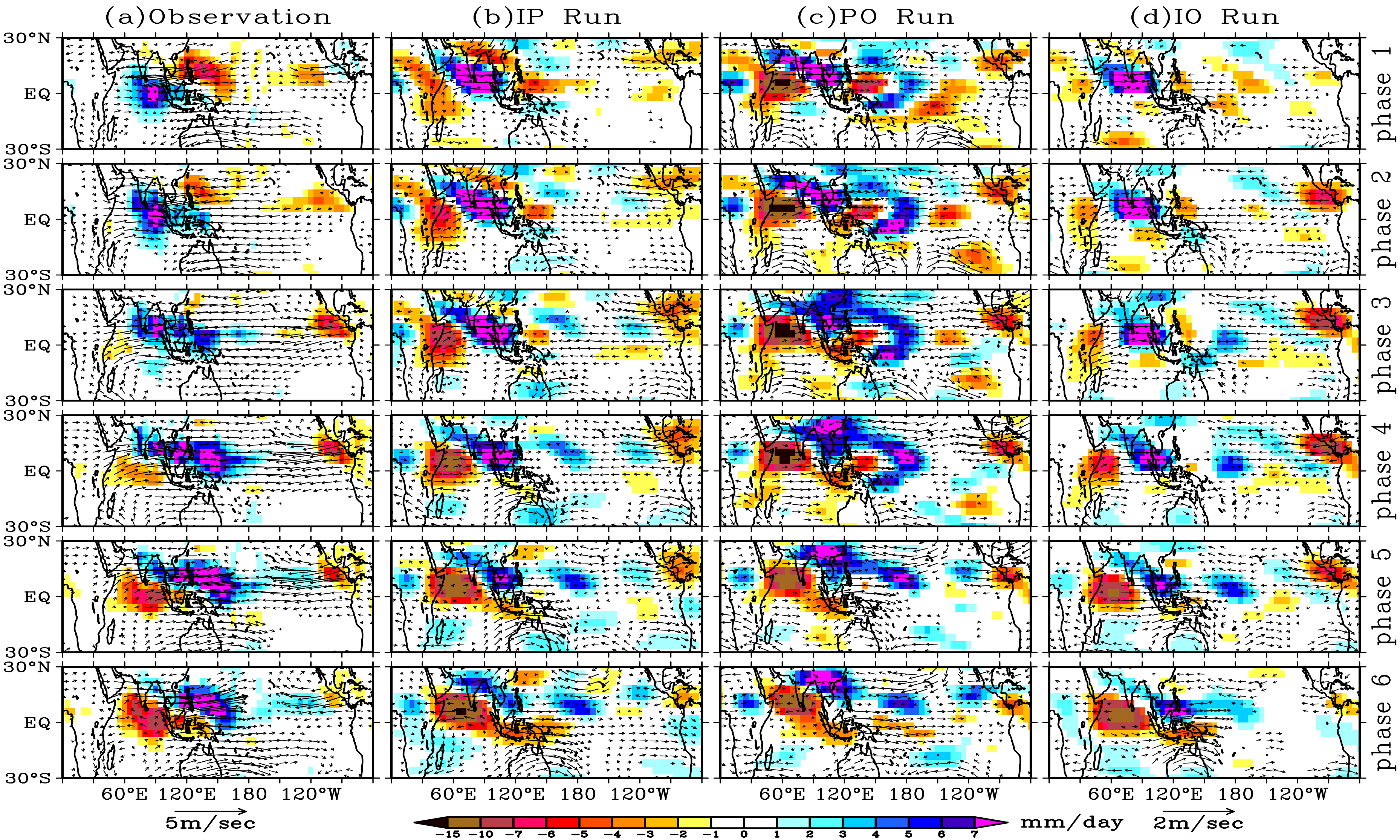

Fig. 10 The summertime (MJJASO) ISO life cycles in the rainfall and 850-mb wind anomalies are shown for (a) observation, (b) IP, (c) PO, and (d) IO Runs. Only the first half of the life cycle from phase 1 (-25 day) to phase 6 (+0 day) are shown. Color-shaded areas and the black vectors denote the rainfall and wind anomalies significant at 95% (90%) confidence level, respectively. Note that the different scales are used between observed and simulated wind anomalies.

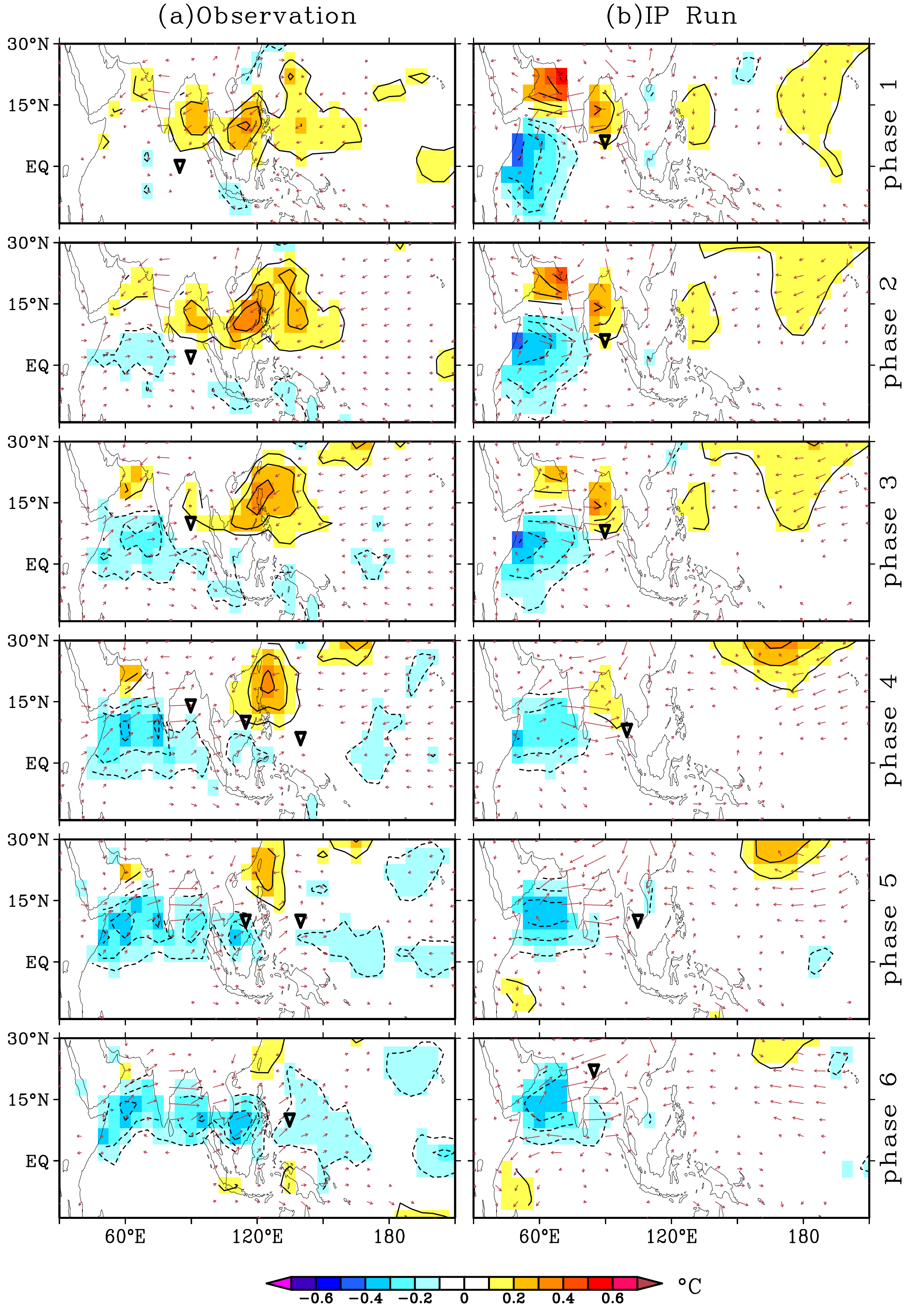

Fig. 11 The configurations are the same as those in Fig. 7, except for the MJJASO period. The centers of enhanced rainfall anomalies in Figs. 10a and 10b are marked as open triangles here. Note that the same scale is used for SST anomalies in observation and IP Run..

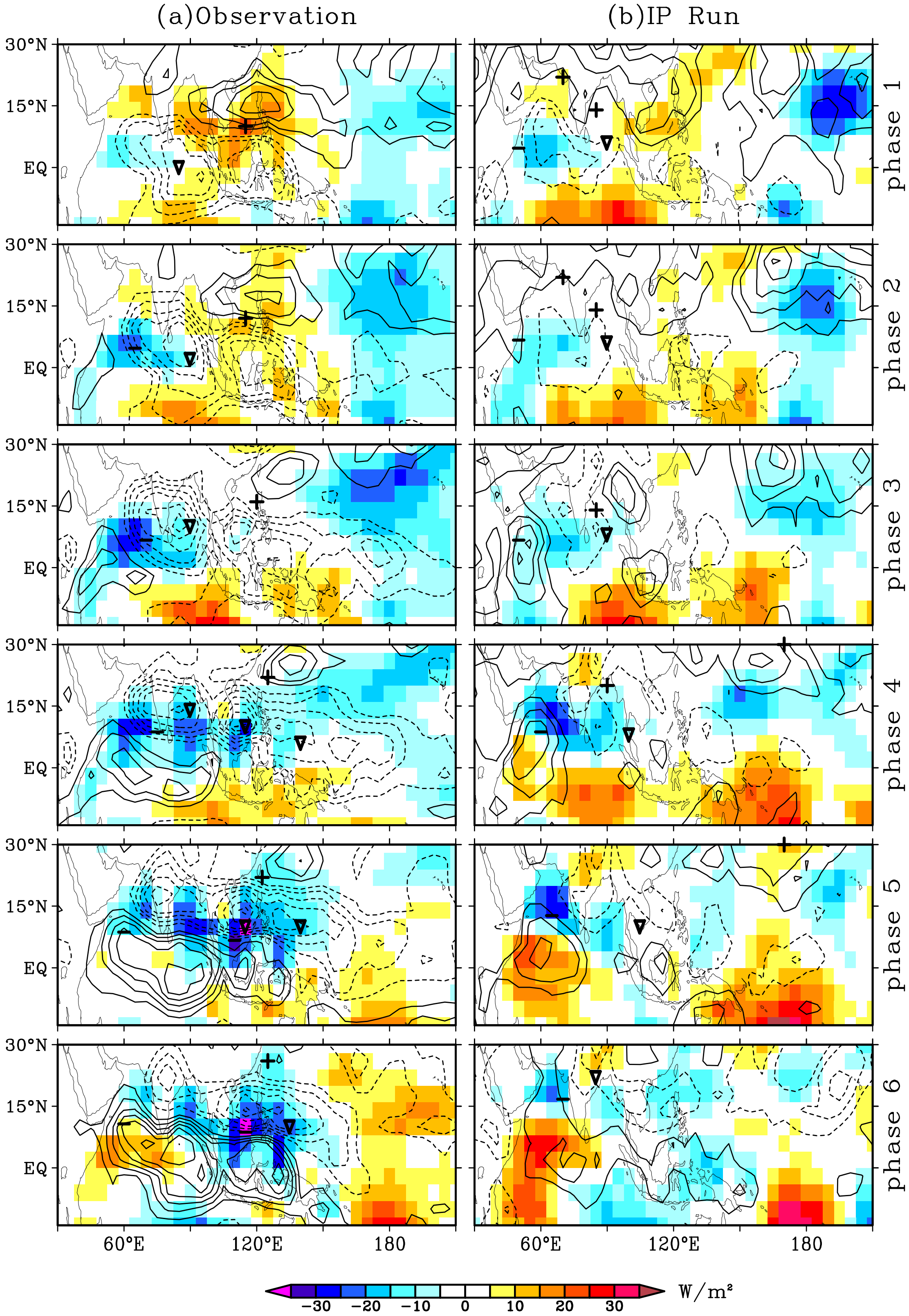

Fig. 12 The configurations are the same as those in Fig. 8, except for the MJJASO period. Enhanced rainfall (in Fig.10a, b) and positive/negative SSTA (in Fig. 11) centers are marked as open triangles and +/−, respectively. Note that the same scale is used in both observed and simulated anomalies. The contour interval of SWR anomalies is 5.0 W/m^2.

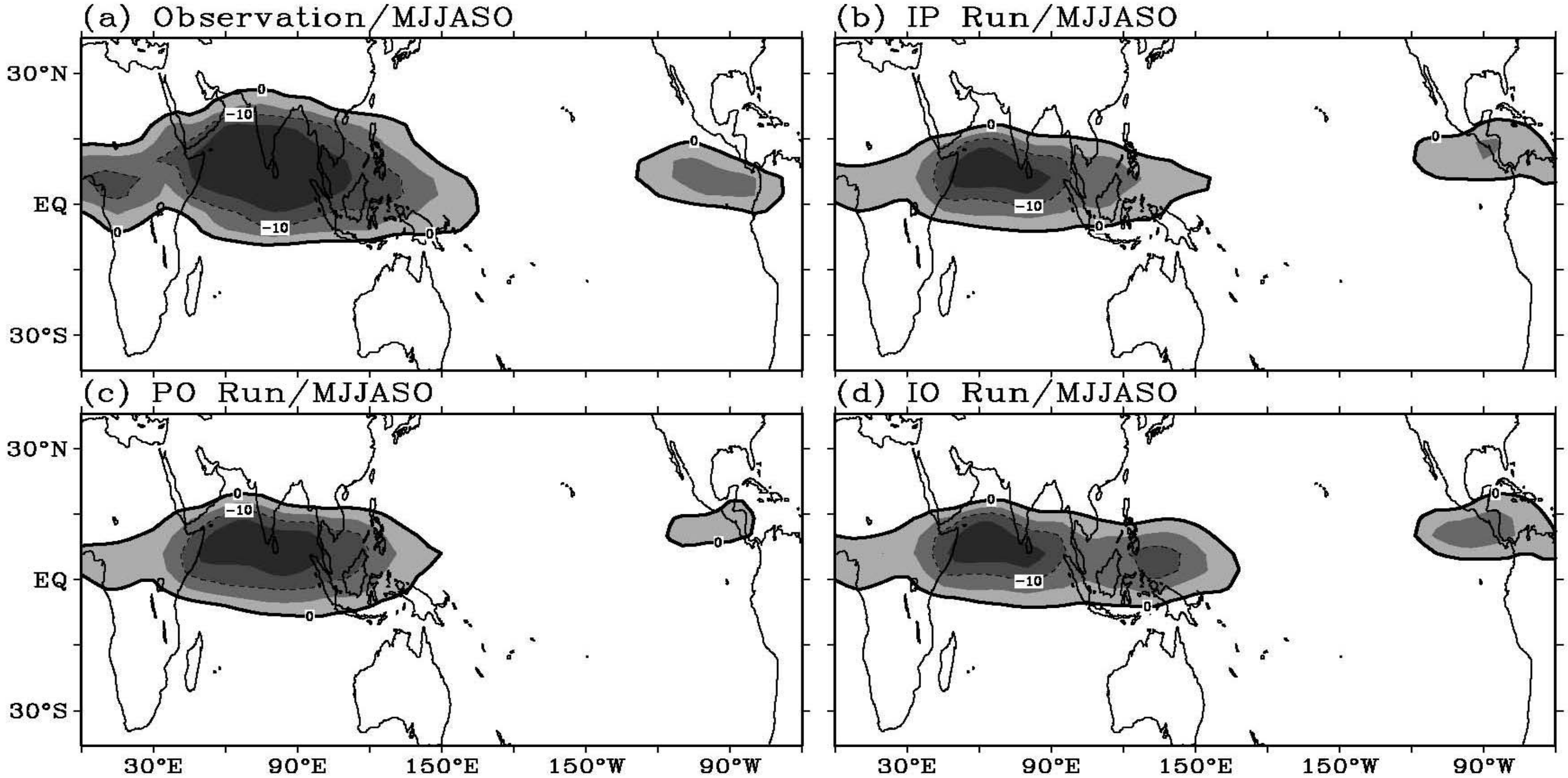

Fig. 13 (a) The observation, (b) IP Run, (c) PO Run, and (d) IO Run simulated mean EVS in MJJASO. Only negative values of EVS are shaded and contoured with 5 m · sec^{-1} intervals.

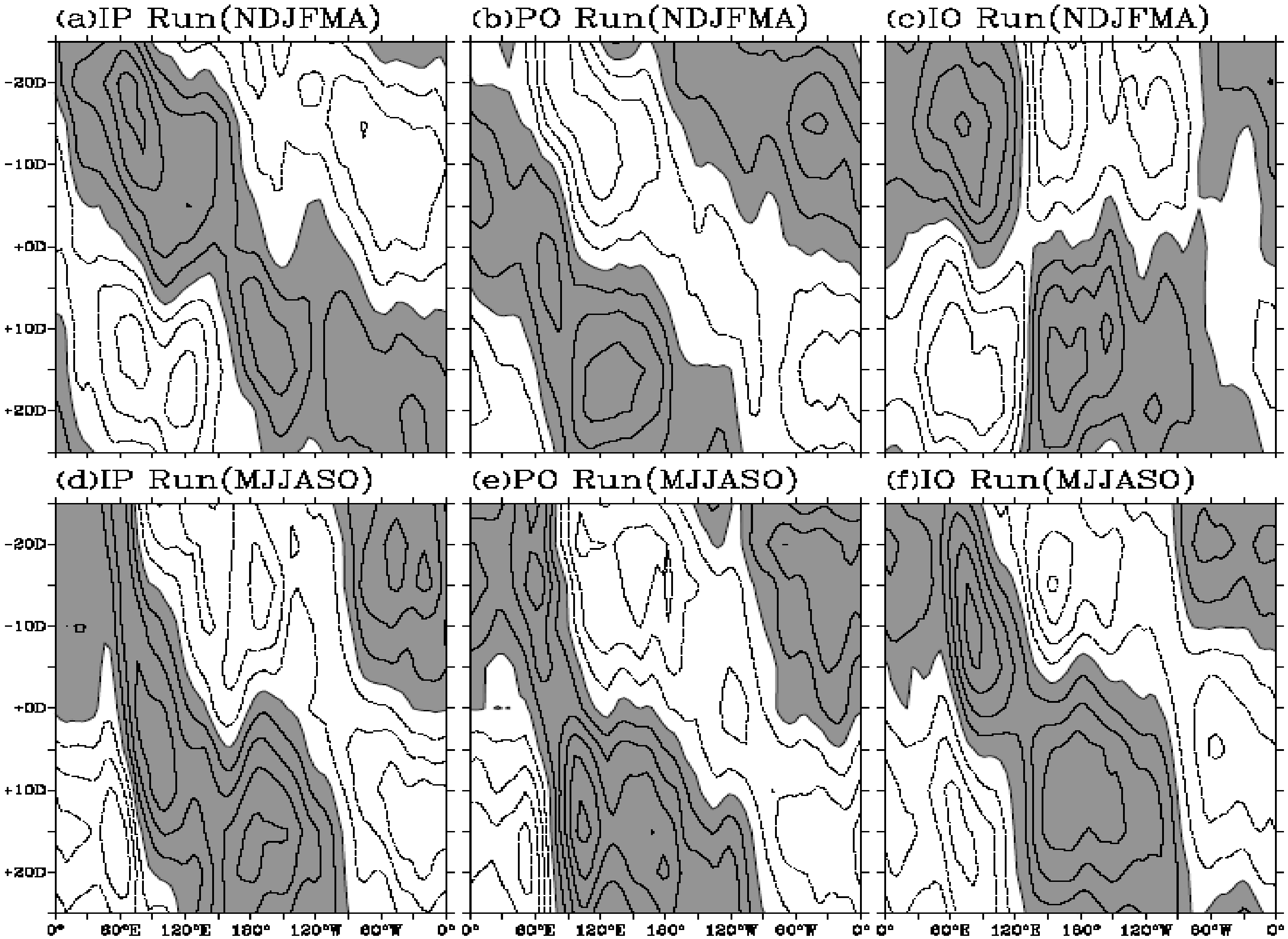

Fig. 14 The Hovmöller diagrams of the compositing χ'_{200} in the forced experiments of IP [(a) and (d)], PO [(b) and (e)], and IO [(c) and (f)] runs. The upper (lower) 3 panels are for the wintertime (summertime) averaged between 10°S and 10°N (2°S and 14°N). Contour interval is 1/3 x 10^6 $m^2 \cdot sec^{-1}$.

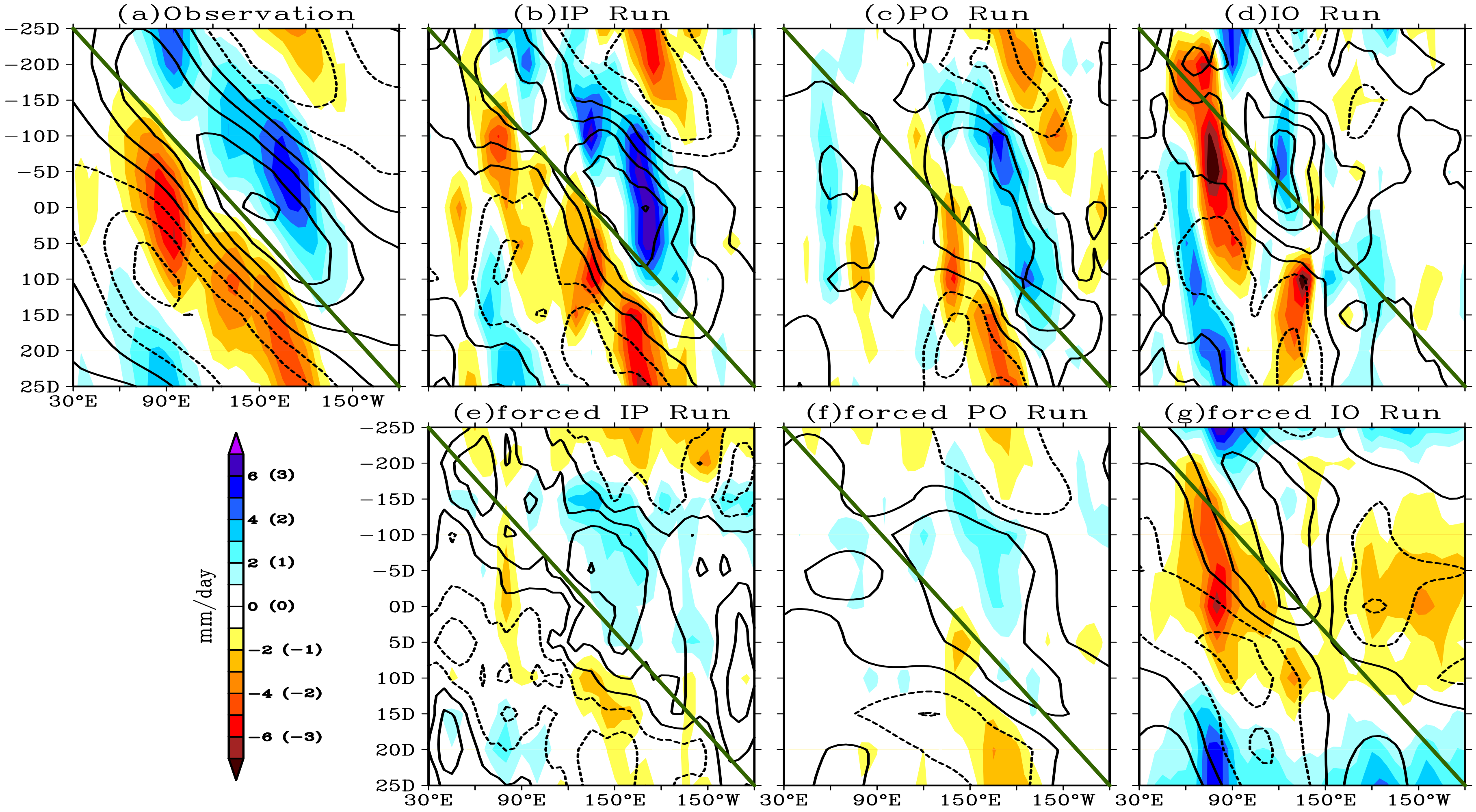

Fig. 15 The Hovmöller diagrams of the wintertime U'_{850} (contour lines; solid: westerly) and rainfall (color shading) composites in the observation (a), 3 coupled runs [(b)-(d)], and 3 forced runs [(e)-(g)]. Anomalies are averaged between 10°S and 10°N. The contour interval of U'_{850} is 1.0 m/sec in panel (a), and 0.5 m/sec elsewhere. Note that the scaling (value inside the parenthesis) used for the simulated rainfall anomalies is only 1/2 of that used for the observations. The straight diagonal lines mark the eastward phase speed around 5 m · sec^{-1}.

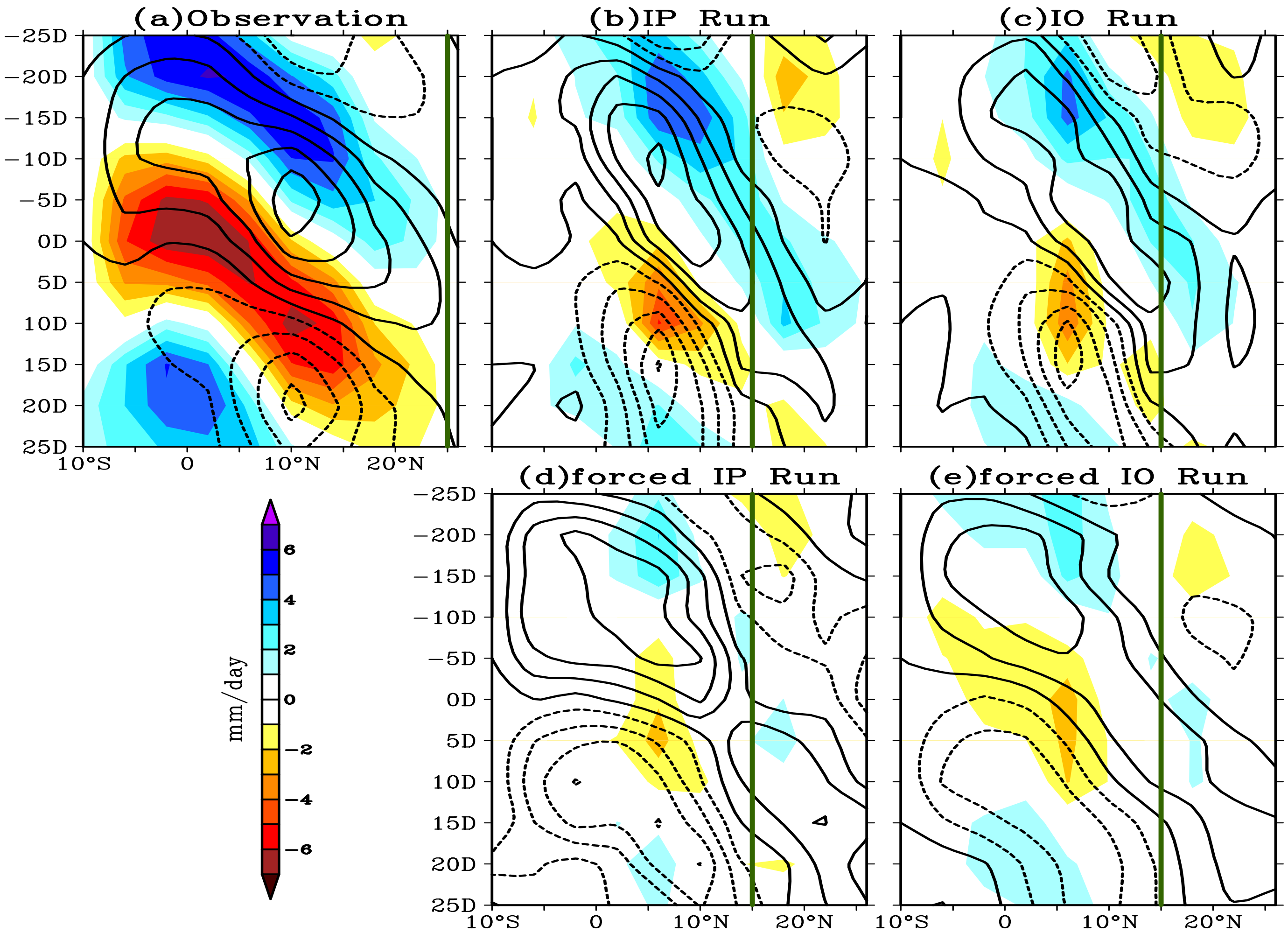

Fig. 16 The time-latitude diagrams of the summertime U'_{850} (contour lines; solid: westerly) and rainfall (color shading) composites in the (a) observation, (b) IP Run , and (c) IO Run, (d) forced IP Run, and (e) forced IO Run. Anomalies are averaged between 85°E and 95°E in the longitudes around Bay of Bengal. Contour interval of U'_{850} is 1.0 m/sec in panel (a), and 0.5 m/sec elsewhere. Vertical green lines mark the averaged locations of zero contours in the seasonal-mean EVS.